

Origin of structural degradation in Li-rich layered oxide cathode

<https://doi.org/10.1038/s41586-022-04689-y>

Received: 8 June 2021

Accepted: 23 March 2022

Published online: 8 June 2022

 Check for updates

Tongchao Liu^{1,10}, Jiajie Liu^{2,10}, Luxi Li^{3,10}, Lei Yu⁴, Jiecheng Diao⁵, Tao Zhou⁴, Shunning Li², Alvin Dai¹, Wenguang Zhao², Shenyang Xu², Yang Ren^{3,9}, Liguang Wang³, Tianpin Wu³, Rui Qi², Yinguo Xiao², Jiaxin Zheng², Wonsuk Cha², Ross Harder², Ian Robinson^{5,6}, Jianguo Wen⁴, Jun Lu^{1,✉}, Feng Pan^{2,✉} & Khalil Amine^{1,7,8,✉}

Li- and Mn-rich (LMR) cathode materials that utilize both cation and anion redox can yield substantial increases in battery energy density^{1–3}. However, although voltage decay issues cause continuous energy loss and impede commercialization, the prerequisite driving force for this phenomenon remains a mystery^{3–6}. Here, with *in situ* nanoscale sensitive coherent X-ray diffraction imaging techniques, we reveal that nanostrain and lattice displacement accumulate continuously during operation of the cell. Evidence shows that this effect is the driving force for both structure degradation and oxygen loss, which trigger the well-known rapid voltage decay in LMR cathodes. By carrying out micro- to macro-length characterizations that span atomic structure, the primary particle, multiparticle and electrode levels, we demonstrate that the heterogeneous nature of LMR cathodes inevitably causes pernicious phase displacement/strain, which cannot be eliminated by conventional doping or coating methods. We therefore propose mesostructural design as a strategy to mitigate lattice displacement and inhomogeneous electrochemical/structural evolutions, thereby achieving stable voltage and capacity profiles. These findings highlight the significance of lattice strain/displacement in causing voltage decay and will inspire a wave of efforts to unlock the potential of the broad-scale commercialization of LMR cathode materials.

Although several prevailing theories have been established for voltage fade, including transition metal (TM) migration, TM valence state reduction and irreversible phase transitions, fade has eventually been attributed to thermodynamic instability of lattice oxygen and to oxygen release^{7–11}. Previous research efforts have also sought diverse solutions to premeditatively enhance lattice oxygen stability; however, the effectiveness of these strategies is limited and this problem remains unresolved so far^{12–15}. This predicament raises the suspicion of whether thermodynamic instability is the governing prerequisite for voltage decay in the Li- and Mn-rich (LMR) cathode.

In conventional intercalation cathodes, Li-ion (Li^+) movement in/out of the host framework will drive dynamic structural evolution, which directly affects structure stability and the electrochemical profile^{16–18}. Unfortunately, uneven Li^+ (de)intercalation and heterogeneous electrochemical reactions often occur in these cathodes, leading to non-equilibrium structural dynamics at both the macroscopic and microscopic levels^{19–21}. The former is manifested as the anisotropic volume variation and bulk mechanical strain, which have been broadly viewed as the root cause of mechanical degradation, such as secondary particle cracking^{22,23}. The latter contributes to nanoscale strain with less detectable lattice

displacement²⁴, in which the destructive effects on topical structure stability remain unclear. This is particularly important for the LMR cathode because its heterogeneous structure is composed of two structurally coherent nanodomains (LiTMO_2 and Li_2MnO_3), which are electrochemically activated in separate voltage ranges with different redox chemistries^{25–27}. It is such heterogeneous structural dynamics of nanodomains that determine the global generation of nanoscale strain, which can substantially alter the structural stability and aggravate oxygen release.

Despite its fundamental importance, lattice displacement and nanoscale strain are probably the least understood structural properties in battery materials. Owing to technical limits faced in the past, characterization tools could not penetrate into nanoscale regimes, preventing the observation of lattice displacement and analysis of nanoscale strain²⁸. It is even more challenging to monitor the spatial strain evolution under *operando* conditions^{20,29,30}. Clearly, building a mechanistic link between nanoscale structure dynamics and electrochemical properties requires systematic investigations spanning multiple length scales, which have the benefit of unifying the previous electrochemical degradation mechanism of LMR cathodes and guiding effective approaches to mitigating voltage fade.

¹Chemical Sciences and Engineering Division, Argonne National Laboratory, Lemont, IL, USA. ²School of Advanced Materials, Peking University, Shenzhen Graduate School, Shenzhen, China. ³X-ray Science Division, Argonne National Laboratory, Lemont, IL, USA. ⁴Center for Nanoscale Materials, Argonne National Laboratory, Lemont, IL, USA. ⁵London Centre for Nanotechnology, University College London, London, UK. ⁶Condensed Matter Physics and Materials Science Department, Brookhaven National Laboratory, Upton, NY, USA. ⁷Materials Science, Energy and Nano-engineering Department, Mohammed VI Polytechnic University (UM6P), Benguerir, Morocco. ⁸Material Science and Engineering, Stanford University, Stanford, CA, USA. ⁹Present address: Department of Physics, City University of Hong Kong, Kowloon, Hong Kong. ¹⁰These authors contributed equally: Tongchao Liu, Jiajie Liu, Luxi Li. [✉]e-mail: junlu@anl.gov; panfeng@pkusz.edu.cn; amine@anl.gov

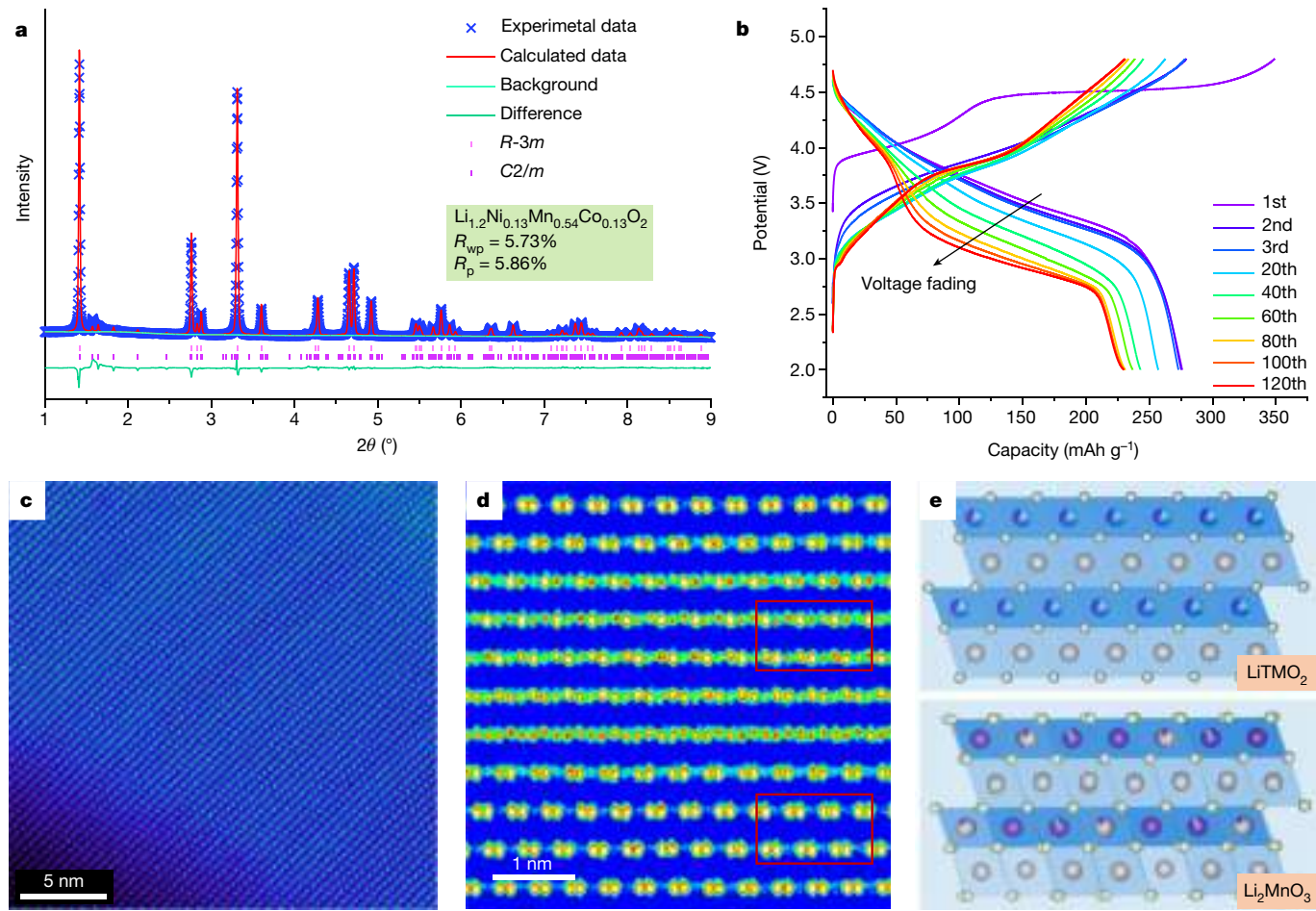


Fig. 1 | Electrochemical profile and initial structure of the LMR cathodes.

a, The X-ray diffraction pattern and Rietveld refinement results of the LMR cathode. **b**, Charge–discharge curves of the LMR cathode within a voltage range of 2.0–4.8 V at 0.1C rate current. **c**, High-resolution TEM image showing the atomic arrangement of the LMR cathode. **d**, Enlarged image of **c**.

Regular ‘bright–bright–dark’ arrangements are identified as Li_2MnO_3 domains, which are characterized by the well-known honeycomb Li–Mn ordering. LiTMO_2 domains are identified with no distinguished dark spots in the bright spot columns. **e**, Schematic structure of LiTMO_2 domains and Li_2MnO_3 domains.

Initial structure/electrochemical properties

A representative LMR cathode with $\text{Li}_{1.2}\text{Ni}_{0.13}\text{Mn}_{0.54}\text{Co}_{0.13}\text{O}_2$ was synthesized by a classical sol–gel method²⁷. Its morphology and composition details are described in the Methods and Extended Data Fig. 1a–f. The X-ray powder diffraction measurement (Fig. 1a) shows identical results to those reported in the literature^{26,27}. Characteristic super-reflections present in the 2θ region 1.4 – 2° correspond to Li/Mn ordering in the TM slabs (Li_2MnO_3 -like phase). Detailed structure information can be found in Extended Data Table 1. Aberration-corrected scanning transmission electron microscopy (AC-STEM) was applied to directly visualize the spatial distribution of LiTMO_2 and Li_2MnO_3 domains. As shown in Fig. 1c–e, it is clear that a typical layered structure is composed of two types of bright spot arrangement. LiTMO_2 domains are three-dimensionally incorporated into the Li_2MnO_3 lattice without obvious interphase boundaries, indicating that these two phases are randomly mixed and share the coherent lattice structure.

The electrochemical profile of the LMR cathode shows a high discharge capacity of 273 mAh g^{-1} but also rapid voltage fade and capacity loss concurrently during cycles (Fig. 1b). Stage 1 is attributed to the activation of LiTMO_2 domains associated with the oxidation of Ni and Co ions³³. Stage 2, at a plateau voltage over 4.47 V , corresponds to the activation of Li_2MnO_3 domains, in which lattice oxygen is oxidized, usually accompanied by

oxygen release^{34,35}. The galvanostatic intermittent titration technique (GITT, Extended Data Fig. 2c, d) further confirms the differential electrochemical activities of these two structurally coherent domains.

It is argued that oxygen-related gas stems from the activation of thermodynamically unstable Li_2MnO_3 domains^{33,36}. Paradoxically, recent results from density functional theory (DFT) calculation demonstrate that oxygen release is thermodynamically unfavourable in the initial delithiation of the pure Li_2MnO_3 ^{37,38}. To clarify the uncertainty shrouding oxygen release, we carefully measure the gas evolution of Li_2MnO_3 using differential electrochemical mass spectrometry (DEMS), in which oxygen-related gas is absent at the initial activation of Li_2MnO_3 around 4.5 V (less than 20% delithiation) and starts to be detected at over 20% delithiation of Li_2MnO_3 (Extended Data Fig. 3a–e). This result provides direct evidence that the activation of pure Li_2MnO_3 material is not the root cause of oxygen release. Consequently, the oxygen release mechanism of the LMR cathode cannot be solely attributed to the activation of domains of Li_2MnO_3 and its thermodynamic instability. The interaction between Li_2MnO_3 and LiTMO_2 , which will lead to non-equilibrium structural responses, is critical for oxygen release, but it seems to have been overlooked previously and has rarely been investigated due to the characterization limit.

Strain evolution observed through BCDI

Bragg coherent X-ray diffraction imaging (BCDI) is an indispensable tool to visualize structural, morphological and lattice strain information in

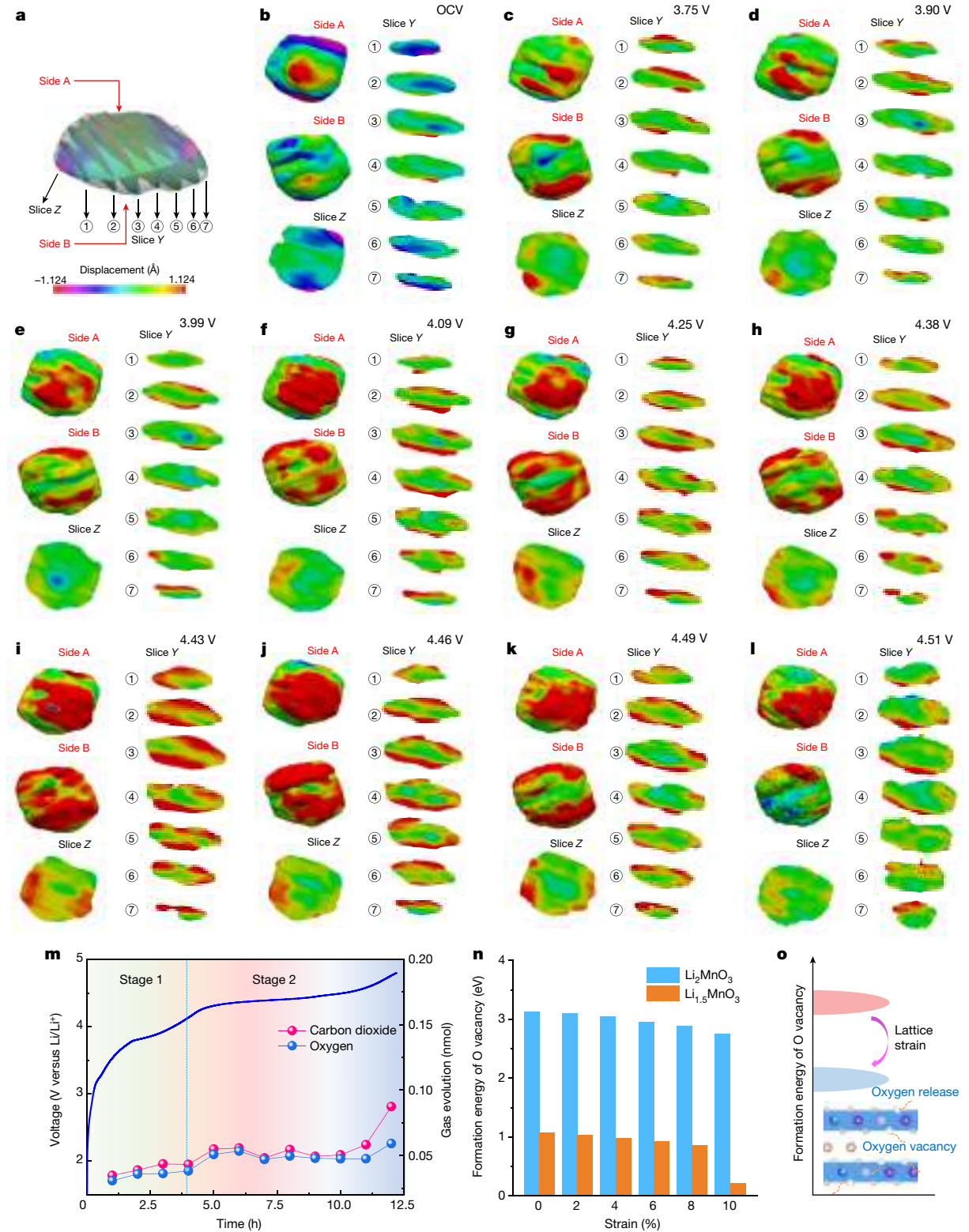


Fig. 2 | Strain evolution of the LMR primary particle and its relationship with oxygen release. **a–l**, In situ (a) BCDF images of the 3D LMR particle in the strain field, measured at 3.2 V (OCV) (b), 3.75 V (c), 3.90 V (d), 3.99 V (e), 4.09 V (f), 4.25 V (g), 4.38 V (h), 4.43 V (i), 4.46 V (j), 4.49 V (k) and 4.51 V (l). The compressive and tensile strains are expressed by blue and red colours,

respectively. The strain evolution in each state is detailed by the spatial location of the slices along the y axis. **m**, In situ differential electrochemical mass spectroscopy measurements for the LMR primary particle. **n**, Formation energy of O vacancies in Li_2MnO_3 and $\text{Li}_{1.5}\text{MnO}_3$ when tensile strains are applied. **o**, Schematic illustration of the influence of lattice strain on O release.

electrode materials^{24,39,40}. In situ BCDF measurements were performed to monitor lattice displacement and analyse strain evolution of the LMR primary particle during electrochemical reactions. The experimental

set-up and data analysis are illustrated in the Methods. Henceforth in this work, we will refer to images of this lattice displacement as generic ‘strain’, although it is technically an integral of strain²⁴.

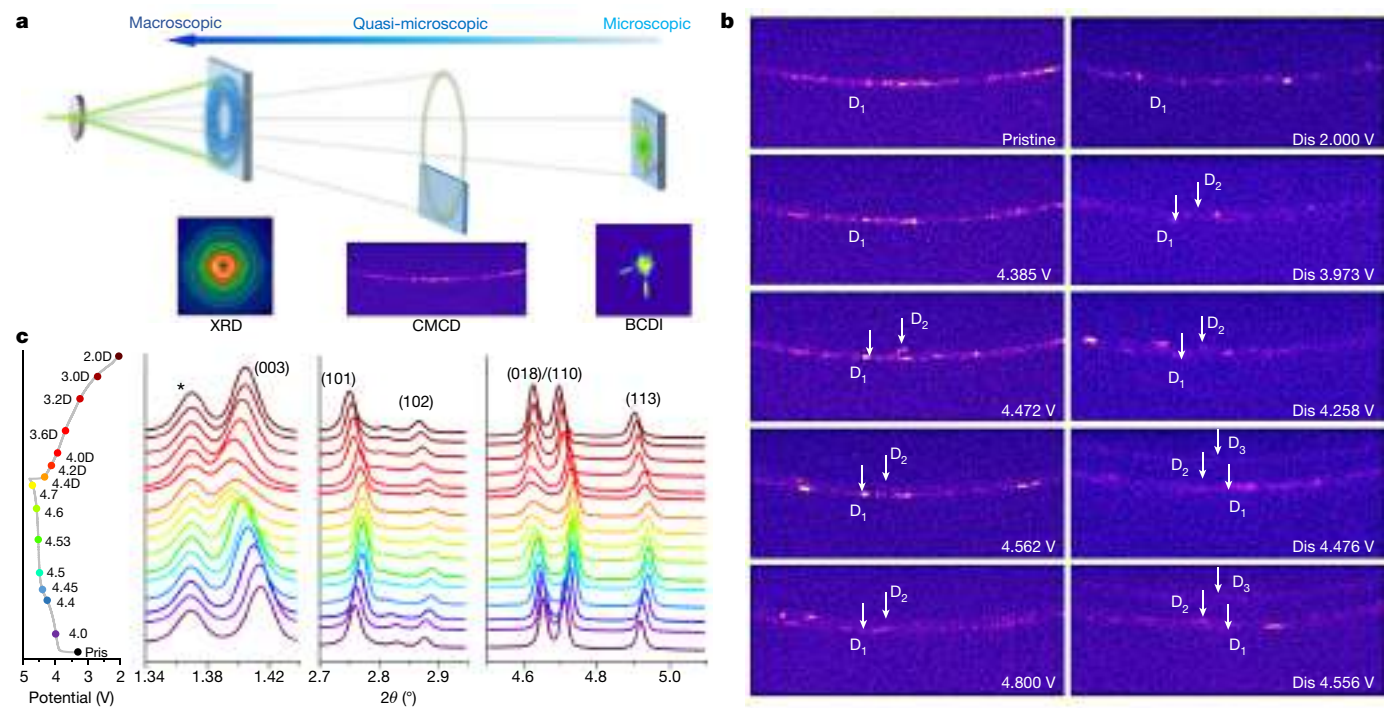


Fig. 3 | Multiscale X-ray diffraction techniques used to investigate the structure evolution of the LMR cathode. **a**, Schematic of multiscale X-ray diffraction (XRD) techniques used in this work. **b**, In situ CMCD for the Debye–Scherrer ring of the (003) peak along with charge and discharge (Dis) curves of the LMR cathode. With just tens of particles giving diffraction signals, CMCD can record semi-statistical information on the structure transmissions of LMR

particles and the response of individual crystals, which are typically not visible in conventional X-ray diffraction. Bright spots in the left column show initial multicrystal diffraction corresponding to tens of particles. D_1 , D_2 and D_3 correspond to three lattice distances. **c**, Ex situ HEXRD of the LMR cathode measured at different potentials. The peak marked by * comes from the polytetrafluoroethylene binder.

In Fig. 2a, to demonstrate the spatial lattice evolution, the reconstructed LMR primary particle is displayed as three-dimensional cross-section images. In the pristine stage (Fig. 2b), we observed the concurrent appearance of both compressive and tensile strain. We believe these initial strains are due to local Li aggregation and vacancies caused by the high-temperature sintering process. The initial strain gradually disappears with initial delithiation as rearrangement of Li occupancies in Li layers occurs (Fig. 2c). When entering the first voltage slope around 3.9 V (Fig. 2d), a tensile strain begins to present itself on the particle surface. As discussed above, the initial Li extraction predominately occurs in the LiTMO_2 domains and results in local lattice expansion. The lattice expansion is partly confined by the inactive Li_2MnO_3 , which results in tensile strain at nanoscale. The tensile strain occurs preferentially near the particle surface area, which makes sense as Li extraction starts there. With continuous Li extraction, the tensile strain gradually accumulates and extends into the interior of the particle (Fig. 2e–h). At the end of stage 1 (4.43 V), in which almost all LiTMO_2 domains are fully delithiated, the electrostatic repulsion between oxygen layers reached the maximum, resulting in the existence of tensile strain in the entire particle (Fig. 2i). Therefore, undergoing such inhomogeneous Li concentration and accumulated tensile strain severely affects the structural stability of the composite LMR cathodes, which may trigger the decomposition of Li_2MnO_3 domains.

Interestingly, the lattice strain evolution reverses on entering stage 2. Figure 2j shows that the tensile strain started to decrease at 4.46 V, which is considered the starting voltage of the Li_2MnO_3 domain activation and the onset of O_2 release. To verify this, in situ DEMS was carried out to measure the gas generation during the first charge. Figure 2m shows that oxygen-related gas did not evolve in stage 1. On entering stage 2, onset of the O_2 and CO_2 signals were simultaneously observed, which is consistent with the strain changes mentioned above⁴¹. The overall tensile strain gradually decreased with oxygen release in

stage 2 (Fig. 2k, l), until the particles disappeared from the detection field over 4.51 V. As a consequence, the correlation between lattice strain evolution and oxygen release is naturally established. The inhomogeneous electrochemical kinetics of two domains results in the global existence of tensile strain in the coherent lattice and tremendous inhomogeneity in the Li^+ concentration, which will accelerate the decomposition of Li_2MnO_3 and trigger oxygen release. After oxygen release, the confined lattice expansion relaxes and in turn leads to decrease in lattice strain. This argument is further supported by the results of the DFT calculation. Figure 2n, o indicates that the energy barriers to remove lattice oxygen will be significantly reduced when the increased lattice strain is applied to the Li_2MnO_3 domains.

Origin and relaxation of tensile strain

Systematic structure characterization at multilength scales was performed to investigate LMR structure evolution during the first cycle (Fig. 3a) and link lattice displacement/nanostrain with electrochemical reaction. The in situ coherent X-ray multicrystal diffraction (CMCD) technique was initially applied to monitor minuscule LMR phase evolutions during operando operation⁴¹. This technique provides unique observations that lie between macroscopic and microscopic views and which fill the gap between conventional X-ray diffraction and BCDI. In Fig. 3b, the image captured at the open circuit voltage (OCV) shows a single ring composed of sequential bright diffraction spots (D_1), which correspond to c axis reflections of tens of primary particles. As single-phase reaction in LiTMO_2 domains occurs below 4.47 V, no obvious Debye–Scherrer ring changes occur. At 4.472 V, when oxygen release begins, a bright diffraction spot appears at a smaller angle (D_2), which suggests that part of a particle undergoes lattice expansion with oxygen release. This reaction is attributable to activation of Li_2MnO_3 domains and leads to the relaxation of the confined lattice. The D_2

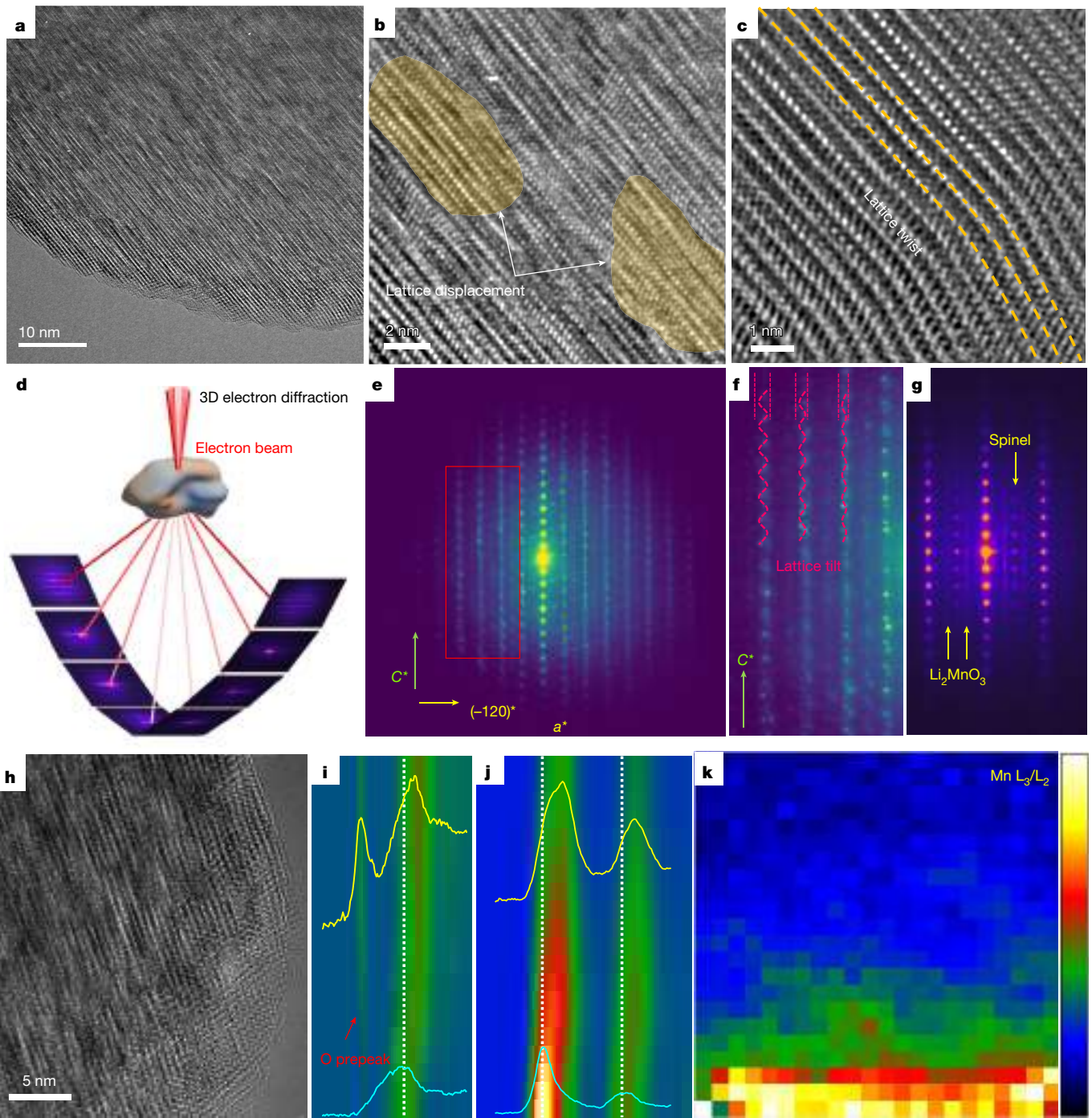


Fig. 4 | Visible observation from atomic-level TEM, 3D electron diffraction and chemical state analysis from EELS. **a**, Low-magnification TEM image of the LMR cathode charged to 4.47 V. **b**, Enlarged image of the LMR particle's bulk area. **c**, High-resolution TEM image of the LMR surface. **d**, Schematic of the data collection process of 3D-rED. **e**, Reciprocal lattice along the a^* -axis of the LMR cathode. **f**, Enlarged image of the selected area in **e**. **g**, SAED image of

delithiated sample (4.5 V) at a certain angle of rotation. **h**, Low-magnification TEM image of the LMR cathode charged to 4.8 V. **i,j**, EELS line-scan of O K edge (**i**) and Mn L_{2,3} edge (**j**) of the LMR cathode charged to 4.8 V. **k**, 2D EELS mapping of Mn L₃/L₂. The high value and low value coloured by red and navy blue correspond to lower and higher valence states of Mn, respectively.

ring intensity increases between the oxygen redox plateau and the complete charge until reaching a maximum at 4.8 V; meanwhile, the original powder ring (D_1) weakens as the new powder ring intensifies. These CMCD results clearly show inhomogeneous lattice expansion in the LMR cathode during the first charge. In stage 1 (below 4.472 V), due to the surrounding inactive Li_2MnO_3 domains, the lattice expansion is partly confined and only presents one diffraction ring. Such an inhomogeneous structure evolution of two domains is the primary

cause of the tensile strain observed in the BCDI images. As tensile strain gradually reaches the limit, Li_2MnO_3 domains struggle with the imposed lattice strain and the Li^+ concentration imbalance, which subsequently triggers Li_2MnO_3 decomposition. The confined lattice expansion is released naturally with activation of the Li_2MnO_3 domains, leading to relaxation of the tensile strain.

During discharge, reflections in CMCD images convert back to a single diffraction ring (D_1) via sequential converse structure transitions.

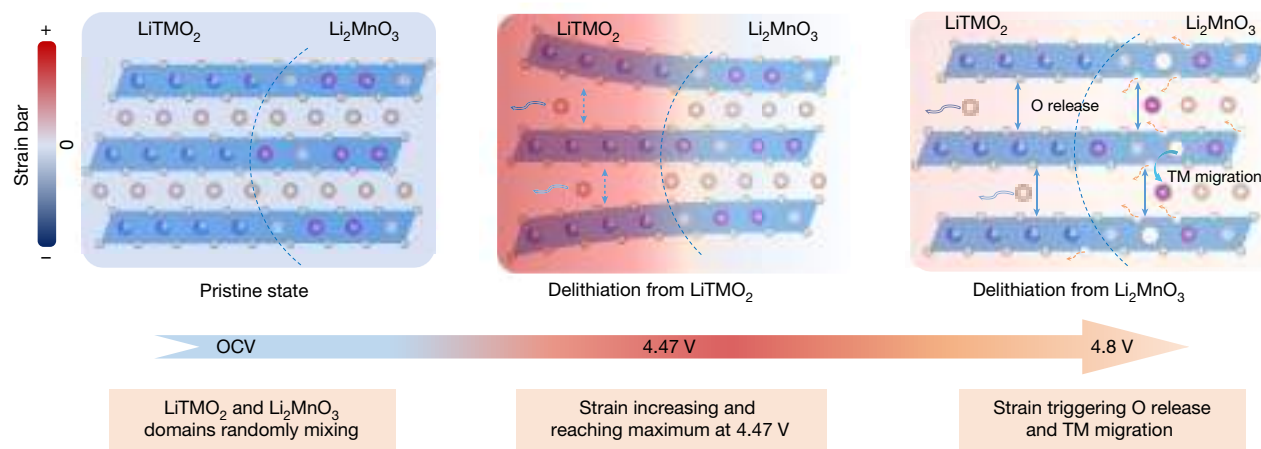


Fig. 5 | Schematic of the correlation of strain generation and O release as well as transition metal migration. The LiTMO_2 and Li_2MnO_3 domains share a coherent lattice at the nanoscale but exhibit differentiated electrochemical activities due to different redox chemistries. The initial Li extraction predominately occurs in the LiTMO_2 domains and results in local lattice expansion. The lattice expansion is partly confined by the inactive Li_2MnO_3 ,

which results in tensile strain at the nanoscale. The accumulated tensile strain severely affects the structural stability of the composite LMR cathode, which may trigger the decomposition of Li_2MnO_3 domains, oxygen release and transition metal (TM) migration. The activation of Li_2MnO_3 and oxygen release in turn release the lattice strain at high voltages.

Interestingly, in addition to D_2 and D_1 rings, another weak diffraction ring (D_3) is visualized at an even smaller angle at the start of discharge. This diffraction ring can be indexed to the (101) crystal plane of $\text{Li}_2\text{Mn}_2\text{O}_4$, which is considered to be the phase formed by over-lithiation of spinel $\text{Li}_x\text{Mn}_2\text{O}_4$. This observation implies that TM migration to Li layers occurs with oxygen release and the $\text{Li}_x\text{Mn}_2\text{O}_4$ spinel-like phase forms during the first charge. The D_3 diffraction ring only appeared in the first 10 min of discharge (versus a total of 10 h discharge time), which suggests $\text{Li}_2\text{Mn}_2\text{O}_4$ is a kinetic-dependent intermediate phase. In this sense, we infer that $\text{Li}_x\text{Mn}_2\text{O}_4$ -like spinel domains probably concentrate on particle surfaces that are momentarily over-lithiated due to the high surface Li-ion concentration and poor Li diffusion of the surface when discharge initiates. As lithium ions gradually migrate to the bulk, the over-lithiated $\text{Li}_2\text{Mn}_2\text{O}_4$ gradually change to LiMn_2O_4 , for which the diffraction ring is very close to D_1 and D_2 . Thus, the D_3 diffraction ring accordingly disappears with surface Li^+ concentration equilibrium.

Concurrently, high-energy in situ and ex situ X-ray diffraction was conducted to investigate macroscopic structural evolution. Figure 3c and Extended Data Fig. 4a, b show a (003) peak shift towards lower diffraction angles before 4.45 V, which is associated with lattice expansion induced by LiTMO_2 domains. When charged to 4.45 V, obvious (003) peak broadening propagates, indicating that the confined lattice expansion is released with decomposition of Li_2MnO_3 domains. These statistical observations of structure evolution are consistent with the appearance of the second diffraction ring (D_2) in the CMCD images. At the same time, the disappearance of the superlattice peak over 4.5 V suggests that TM migration must occur with oxygen release, and TM ordering is broken. This argument is further supported by ex situ extended X-ray absorption fine structure (EXAFS) and the fitting results. Extended Data Fig. 4c–e and Extended Data Table 2 show that the coordination number of Mn–O decreases, but that of Mn–TM increases accordingly, suggesting that lattice strain accumulation will trigger TM migration and oxygen release. More importantly, the broadening and weakening of a series of peaks are found to be mainly related to the c axis, such as (003), (104), (107) and (108) peaks (Fig. 3c and Extended Data Fig. 4a). The oriented peak broadening is due to more inhomogeneous lattice changes occurring mainly along the c axis during charge/discharge, which further confirmed that strain evolution stems from the heterogeneous nature of the LMR cathode.

Atomic observation of lattice displacement

Transmission electron microscopy (TEM), three-dimensional (3D) rotation electron diffraction (3D-rED) and electron energy loss spectroscopy (EELS) were performed on delithiated samples to investigate lattice displacement and nanostructure evolution. As mentioned, inhomogeneous electrochemical activities and structure evolution result in nanoscale strain. At micro scales, strain is manifested as lattice displacement, which can be captured by high-resolution TEM (HRTEM). Figure 4a–c and Extended Data Fig. 5 show that, although a layered structure is maintained at 4.47 V, obvious surface and bulk lattice displacements are present. Lattices in the marked areas are deformed significantly. These displacements occur predominantly on surfaces with constant lattice twists (Fig. 4c), which can be attributed to concentrated surface strain.

During stage 2, continuous delithiation is accompanied by oxygen release and Li_2MnO_3 domain activation. Identical observations were carried out to track these changes after Li_2MnO_3 activation. Extended Data Fig. 6a–m shows that, besides lattice displacement, a phase transition from a layered structure to the spinel phase occurs in this stage (4.5 V). Lattice evolution at larger scales was investigated by 3D-rED in reciprocal space (Fig. 4d and Extended Data Fig. 7)⁴². Reconstructed discrete reciprocal lattices (Fig. 4e, f and Extended Data Fig. 8a, b) clearly show twisted reflections along the c axis, which could be attributed to the lattice displacement observed in the HRTEM. Figure 4g and Extended Data Fig. 8c–g show selected area electron diffraction with a typical layered structure, weak Li_2MnO_3 reflections and a new reflection corresponding to the spinel lattice. This verifies that severe lattice strain triggers TM migration and structure transition from the layered phase to the spinel phase, which agrees with the structure evolution captured by CMCD.

TEM combined with EELS was used to precisely probe the structural and chemical variation of the fully delithiated sample (4.8 V). Figure 4h and Extended Data Fig. 9a, b confirm the structure transitions, especially on the particle surface. Clear reconstruction of surface layers with spinel and rock-salt phases provides direct evidence of TM migration and irreversible phase transition after oxygen release. The O K edge and Mn $L_{2,3}$ EELS line profiles were stacked in Fig. 4i, j and Extended Data Fig. 9c from the bulk to surface. The O K edge pre-peak intensities decrease from the interior to the exterior, and almost disappear near the surface. The O K edge line scans that are parallel to the surface (Extended Data Fig. 9d) further confirm that oxygen release uniformly

occurs in the whole particle surface as the O pre-peak disappears. It is notable that oxygen release predominately occurs near surfaces, where strain evolves most drastically during initial charge, verifying that strain accumulation is the root cause of oxygen release. Concurrently, Mn L edges shift to the left near surfaces (Fig. 4j). Two-dimensional (2D) EELS mapping further shows the chemical state change of Mn in the entire particle (Fig. 4k), where the surface reconstruction layer shows a lower Mn valence than the bulk, which suggests that the Mn oxidation state decreases with migration and oxygen release near the surface. These observations demonstrate how oxygen release and TM migration occur preferentially in regions where structures experience severe lattice strain.

A prospect for LMR cathode development

Although the fact that oxygen release or vacancies are generated extensively in the bulk, and aggravate structural/electrochemical degradation, has been recognized recently, the driving force remains unclear^{43–45}. TM migration and irreversible phase transition also remain localized to surfaces in TEM observations, and unobservable in macroscopic characterizations^{46–48}. Therefore, it is questionable as to whether such local structural degradation can undermine the overall electrochemical behaviour. Here, our work details dynamic nanostructure evolution and local structure interaction that were previously unobservable. With multiscale characterizations and DFT calculation, lattice displacement/strain that are induced by non-equilibrium structural dynamics are found to be the driving force for voltage fade. Consequently, nanoscale strain evolution provides a plausible explanation for the origin of oxygen release and TM migration, thus unifying previous theories for voltage fade.

The strain-induced structure degradation is detailed schematically in Fig. 5. Generally, different electrochemical reactivities but coherent lattice structures for two domains constitute a prerequisite for lattice strain. LiTMO₂ activation increases local electrostatic repulsion with a tendency for lattice expansion. By contrast, due to the inactive O redox of Li₂MnO₃ domains, their lattice expansion is partly confined, resulting in severe nanoscale strain with lattice displacement. Lattice strain initiates from the particle surface, gradually extends into the bulk with continuous delithiation and peaks when LiTMO₂ domains reach near-total delithiation. These extreme strains substantially destabilize structures, and trigger Li₂MnO₃ decomposition with oxygen release. When Li₂MnO₃ domains are activated, the imposed lattice expansion is naturally released and tensile strain relaxes synchronously. Similarly, oxygen release also significantly lowers TM migration energy barriers, resulting in irreversible phase transition⁴⁹. Such strain evolution would adversely accumulate on long-term cycling, and inevitably cause structural degradation and fast electrochemical decay.

Therefore, heterogeneous composite structures with different electrochemical activities are found to cause lattice strain in the LMR cathode. This explains why post treatments, such as surface engineering methods, are ineffective for voltage decay. To resolve this issue, practical solutions for these lattice strain challenges must address heterogeneous structures in the LMR cathodes and their differential electrochemical activities, which requires fundamental consideration of composition design or local structure regulation. Altering the domain mesostructure in O3-type LMR cathodes has been challenging, so we attempted to eliminate composite domain structure with homogeneous atomic arrangement in O2-type LMR cathodes. Extended Data Fig. 10a, b shows an O2-type Li_xNi_{0.13}Mn_{0.54}Co_{0.13}O₂ cathode that eliminates the composite domain structure with homogeneous atomic arrangement. Notably, the differential electrochemical activities are effectively suppressed, as evidenced by the smooth charging behaviour with no differentiated voltage plateau (Extended Data Fig. 10c, d). Therefore, well-integrated electrochemical activities in the O2-based cathode eliminate the prerequisite for strain generation, inhibit oxygen

release and achieve enhanced electrochemical performance with stable voltages. This proves that addressing lattice strain is essential to solve voltage fade, a long-standing issue. Other realistic strategies based on electrochemical reactivity are similarly promising. It is ideal if two redox reactions can be completely blended to realize cationic/anionic hybrid redox in the cathode across wide voltage ranges. This could not only eliminate inhomogeneous reactivity across two domains, but also access higher energy density, which potentially carries forward the practical application of anionic redox or cationic/anionic hybrid cathode materials.

Online content

Any methods, additional references, Nature Research reporting summaries, source data, extended data, supplementary information, acknowledgements, peer review information; details of author contributions and competing interests; and statements of data and code availability are available at <https://doi.org/10.1038/s41586-022-04689-y>.

- Li, M. et al. Cationic and anionic redox in lithium-ion based batteries. *Chem. Soc. Rev.* **49**, 1688–1705 (2020).
- Hu, E. et al. Evolution of redox couples in Li- and Mn-rich cathode materials and mitigation of voltage fade by reducing oxygen release. *Nat. Energy* **3**, 690–698 (2018).
- Assat, G. & Tarascon, J.-M. Fundamental understanding and practical challenges of anionic redox activity in Li-ion batteries. *Nat. Energy* **3**, 373–386 (2018).
- Sathiya, M. et al. Reversible anionic redox chemistry in high-capacity layered-oxide electrodes. *Nat. Mater.* **12**, 827–835 (2013).
- Zheng, J. et al. Li-and Mn-rich cathode materials: challenges to commercialization. *Adv. Energy Mater.* **7**, 1601284 (2017).
- Choi, J. W. & Aurbach, D. Promise and reality of post-lithium-ion batteries with high energy densities. *Nat. Rev. Mater.* **1**, 16013 (2016).
- Sathiya, M. et al. Origin of voltage decay in high-capacity layered oxide electrodes. *Nat. Mater.* **14**, 230–238 (2015).
- Pearce, P. E. et al. Evidence for anionic redox activity in a tridimensional-ordered Li-rich positive electrode β -Li₂IrO₃. *Nat. Mater.* **16**, 580–586 (2017).
- Hong, J. et al. Metal-oxygen decoordination stabilizes anion redox in Li-rich oxides. *Nat. Mater.* **18**, 256–265 (2019).
- Hu, S. et al. Insight of a phase compatible surface coating for long-durable Li-rich layered oxide cathode. *Adv. Energy Mater.* **9**, 1901795 (2019).
- Shang, H. et al. Suppressing voltage decay of a lithium-rich cathode material by surface enrichment with atomic ruthenium. *ACS Appl. Mater. Interfaces* **10**, 21349–21355 (2018).
- Singer, A. et al. Nucleation of dislocations and their dynamics in layered oxide cathode materials during battery charging. *Nat. Energy* **3**, 641–647 (2018).
- Yan, P. et al. Injection of oxygen vacancies in the bulk lattice of layered cathodes. *Nat. Nanotechnol.* **14**, 602–608 (2019).
- Assat, G. et al. Fundamental interplay between anionic/cationic redox governing the kinetics and thermodynamics of lithium-rich cathodes. *Nat. Commun.* **8**, 2219 (2017).
- Luo, K. et al. Charge-compensation in 3d-transition-metal-oxide intercalation cathodes through the generation of localized electron holes on oxygen. *Nat. Chem.* **8**, 684–691 (2016).
- Liu, T. et al. Understanding Co roles towards developing Co-free Ni-rich cathodes for rechargeable batteries. *Nat. Energy* **6**, 277–286 (2021).
- Liu, T. et al. Correlation between manganese dissolution and dynamic phase stability in spinel-based lithium-ion battery. *Nat. Commun.* **10**, 4721 (2019).
- Xu, C. et al. Bulk fatigue induced by surface reconstruction in layered Ni-rich cathodes for Li-ion batteries. *Nat. Mater.* **20**, 84–92 (2021).
- Xu, Z. et al. Charge distribution guided by grain crystallographic orientations in polycrystalline battery materials. *Nat. Commun.* **11**, 83 (2020).
- Ulvestad, A. et al. Topological defect dynamics in operando battery nanoparticles. *Science* **348**, 1344–1347 (2015).
- Zhang, F. et al. Surface regulation enables high stability of single-crystal lithium-ion cathodes at high voltage. *Nat. Commun.* **11**, 3050 (2020).
- Bi, Y. et al. Reversible planar gliding and microcracking in a single-crystalline Ni-rich cathode. *Science* **370**, 1313–1317 (2020).
- Qian, G. et al. Understanding the mesoscale degradation in nickel-rich cathode materials through machine-learning-revealed strain-redox decoupling. *ACS Energy Lett.* **6**, 687–693 (2021).
- Robinson, I. & Harder, R. Coherent X-ray diffraction imaging of strain at the nanoscale. *Nat. Mater.* **8**, 291–298 (2009).
- Yoon, W.-S. et al. Local structure and cation ordering in O3 lithium nickel manganese oxides with stoichiometry $\text{Li}[\text{Ni}_{x}\text{Mn}_{(2-x)}/3\text{Li}_{(1-2x)/3}\text{O}_2]$: NMR studies and first principles calculations. *Electrochim. Solid-State Lett.* **7**, A167–A171 (2004).
- Yu, H. et al. Direct atomic-resolution observation of two phases in the $\text{Li}_{1.2}\text{Mn}_{0.56}\text{Ni}_{0.16}\text{Co}_{0.06}\text{O}_2$ cathode material for lithium-ion batteries. *Angew. Chem. Int. Ed. Engl.* **52**, 5969–5973 (2013).
- Leifer, N. et al. Linking structure to performance of $\text{Li}_{1.2}\text{Mn}_{0.54}\text{Ni}_{0.13}\text{Co}_{0.13}\text{O}_2$ (Li and Mn rich NMC) cathode materials synthesized by different methods. *Phys. Chem. Chem. Phys.* **22**, 9098–9109 (2020).
- Lin, F. et al. Synchrotron X-ray analytical techniques for studying materials electrochemistry in rechargeable batteries. *Chem. Rev.* **117**, 13123–13186 (2017).

29. Xu, Z. et al. Charging reactions promoted by geometrically necessary dislocations in battery materials revealed by *in situ* single-particle synchrotron measurements. *Adv. Mater.* **32**, 2003417 (2020).
30. Jha, S. K., Charalambous, H., Okasinski, J. S. & Tsakalakos, T. Using *in operando* diffraction to relate lattice strain with degradation mechanism in a NMC battery. *J. Mater. Sci.* **54**, 2358–2370 (2019).
31. Qiu, B. et al. Metastability and reversibility of anionic redox-based cathode for high-energy rechargeable batteries. *Cell Rep. Phys. Sci.* **1**, 100028 (2020).
32. Li, W., Erickson, E. M. & Manthiram, A. High-nickel layered oxide cathodes for lithium-based automotive batteries. *Nat. Energy* **5**, 26–34 (2021).
33. Zhao, S., Yan, K., Zhang, J., Sun, B. & Wang, G. Reaction mechanisms of layered lithium-rich cathode materials for high-energy lithium-ion batteries. *Angew. Chem. Int. Ed. Engl.* **60**, 2208–2220 (2021).
34. Strehle, B. et al. The role of oxygen release from Li-and Mn-rich layered oxides during the first cycles investigated by on-line electrochemical mass spectrometry. *J. Electrochem. Soc.* **164**, A400–A406 (2017).
35. Nakayama, K., Ishikawa, R., Kobayashi, S., Shibata, N. & Ikuhara, Y. Dislocation and oxygen-release driven delithiation in Li_2MnO_3 . *Nat. Commun.* **11**, 4452 (2020).
36. Rana, J. et al. Structural changes in Li_2MnO_3 cathode material for Li-ion batteries. *Adv. Energy Mater.* **4**, 1300998 (2014).
37. Xiao, R., Li, H. & Chen, L. Density functional investigation on Li_2MnO_3 . *Chem. Mater.* **24**, 4242–4251 (2012).
38. Chen, H. & Islam, M. S. Lithium extraction mechanism in Li-rich Li_2MnO_3 involving oxygen hole formation and dimerization. *Chem. Mater.* **28**, 6656–6663 (2016).
39. Li, L., Xie, Y., Maxey, E. & Harder, R. Methods for *operando* coherent X-ray diffraction of battery materials at the Advanced Photon Source. *J. Synchrotron Radiat.* **26**, 220–229 (2019).
40. Robinson, I., Vartanyants, I., Williams, G., Pfeifer, M. & Pitney, J. Reconstruction of the shapes of gold nanocrystals using coherent X-ray diffraction. *Phys. Rev. Lett.* **87**, 195505 (2001).
41. Maiti, S. et al. Understanding the role of alumina (Al_2O_3), pentalithium aluminate (Li_5AlO_4), and pentasodium aluminate (Na_5AlO_4) coatings on the Li and Mn-rich NCM cathode material $0.33\text{Li}_2\text{MnO}_3\text{-}0.67\text{Li}(\text{Ni}_{0.4}\text{Co}_{0.2}\text{Mn}_{0.4})\text{O}_2$ for enhanced electrochemical performance. *Adv. Funct. Mater.* **31**, 2008083 (2021).
42. Li, J. et al. Structural origin of the high-voltage instability of lithium cobalt oxide. *Nat. Nanotechnol.* **16**, 599–605 (2021).
43. Eum, D. et al. Voltage decay and redox asymmetry mitigation by reversible cation migration in lithium-rich layered oxide electrodes. *Nat. Mater.* **19**, 419–427 (2020).
44. House, R. A. et al. First-cycle voltage hysteresis in Li-rich 3d cathodes associated with molecular O_2 trapped in the bulk. *Nat. Energy* **5**, 777–785 (2020).
45. Csernica, P. M. et al. Persistent and partially mobile oxygen vacancies in Li-rich layered oxides. *Nat. Energy* **6**, 642–652 (2021).
46. Liu, H. et al. Unraveling the rapid performance decay of layered high-energy cathodes: from nanoscale degradation to drastic bulk evolution. *ACS Nano* **12**, 2708–2718 (2018).
47. Boulineau, A., Simonin, L., Colin, J. F., Bourbon, C. & Patoux, S. First evidence of manganese-nickel segregation and densification upon cycling in Li-rich layered oxides for lithium batteries. *Nano Lett.* **13**, 3857–3863 (2013).
48. Teufel, T., Strehle, B., Müller, P., Gasteiger, H. A. & Mendez, M. A. Oxygen release and surface degradation of Li- and Mn-rich layered oxides in variation of the Li_2MnO_3 content. *J. Electrochem. Soc.* **165**, A2718–A2731 (2018).
49. Chen, Z., Li, J. & Zeng, X. C. Unraveling oxygen evolution in Li-rich oxides: a unified modeling of the intermediate peroxy/superoxo-like dimers. *J. Am. Chem. Soc.* **141**, 10751–10759 (2019).

Publisher's note Springer Nature remains neutral with regard to jurisdictional claims in published maps and institutional affiliations.

© This is a U.S. government work and not under copyright protection in the U.S.; foreign copyright protection may apply 2022

Methods

Materials synthesis

$\text{Li}_{1.2}\text{Ni}_{0.13}\text{Mn}_{0.54}\text{Co}_{0.13}\text{O}_2$ used in this paper is one of the most representative compositions for Li- and Mn-rich layered oxides and has been frequently used as a model material for understanding mechanism. Synthesis of primary particles, rather than secondary particles, was purposely controlled for minimizing interference from morphological factors. The primary particle cathode materials of $\text{Li}_{1.2}\text{Ni}_{0.13}\text{Mn}_{0.54}\text{Co}_{0.13}\text{O}_2$ were synthesized using a sol-gel method. In a typical synthesis, $\text{LiCH}_3\text{COO} \cdot 2\text{H}_2\text{O}$ (Aladdin, 99%), $\text{Ni}(\text{CH}_3\text{COO})_2 \cdot 4\text{H}_2\text{O}$ (Aladdin, 99%), $\text{Co}(\text{CH}_3\text{COO})_2 \cdot 4\text{H}_2\text{O}$ (Aladdin, 99.5%), $\text{Mn}(\text{CH}_3\text{COO})_2 \cdot 4\text{H}_2\text{O}$ (Aladdin, 99%) and polyvinylpyrrolidone (Aladdin, K30) were mixed in a molar ratio of 9:1:1:4:30 and then dissolved in 100 ml deionized water. The resulting solution was dried at 90 °C overnight under continuous stirring and then calcinated at 500 °C for 3 h. The obtained powder was thoroughly ground and mixed in a mortar and then calcinated at 900 °C for 12 h to obtain the final product. Extended Data Fig. 1a–e shows a single-particle morphology with sizes ranging from 200 to 600 nm, which is an ideal size for the BCDI measurements. Data in Extended Data Fig. 1f confirm that the composition of the as-prepared sample was close to the designed composition.

The O₂ phase-based $\text{Li}_x\text{Ni}_{0.13}\text{Mn}_{0.54}\text{Co}_{0.13}\text{O}_2$ was synthesized using a sol-gel method followed by a low-temperature ion exchange method. $\text{NaCH}_3\text{COO} \cdot 3\text{H}_2\text{O}$ (Aladdin, 99%), $\text{LiCH}_3\text{COO} \cdot 2\text{H}_2\text{O}$ (Aladdin, 99%), $\text{Ni}(\text{CH}_3\text{COO})_2 \cdot 4\text{H}_2\text{O}$ (Aladdin, 99%), $\text{Mn}(\text{CH}_3\text{COO})_2 \cdot 4\text{H}_2\text{O}$ (Aladdin, 99%), $\text{Co}(\text{CH}_3\text{COO})_2 \cdot 4\text{H}_2\text{O}$ (Aladdin, 99%) and polyvinylpyrrolidone (Aladdin, K30) were mixed in a molar ratio of 85:20:13:54:13:370 and then dissolved in 50 ml deionized water. The resulting solution was dried at 90 °C overnight and then calcinated at 500 °C for 3 h. The obtained powder was thoroughly ground and mixed in a mortar and then calcinated at 800 °C for 10 h to obtain the sodium-containing precursor, $\text{Na}_{0.83}\text{Li}_{0.2}\text{Ni}_{0.13}\text{Co}_{0.13}\text{Mn}_{0.54}\text{O}_2$. Note that 20% Li in this precursor mainly occupies the TM layers, and 83% Na occupies the Na layers. Finally, the precursor was subjected to ion exchange in eutectic $\text{LiNO}_3\text{-LiCl}$ at 280 °C for 4 h to obtain $\text{Li}_{0.83}\text{Li}_{0.2}\text{Ni}_{0.13}\text{Mn}_{0.54}\text{Co}_{0.13}\text{O}_2$. To simplify, this can be written as $\text{Li}_{1.03}\text{Ni}_{0.13}\text{Mn}_{0.54}\text{Co}_{0.13}\text{O}_2$.

Electrochemistry tests

For electrode preparation, active materials were mixed with carbon black (C45 Conductive Carbon Black, TIMCAL) and polyvinylidene fluoride (PVDF, 8 wt% Solvay 5130 PVDF binder dissolved in N-methyl-2-pyrrolidone (NMP)) at 80:10:10 wt% ratios, followed by grinding the mixture in a mortar at 2,000 r.p.m. for 9 min (for 3 times 3 min) in an air atmosphere. The slurry was coated onto 10 μm thick Al foil and then punched into round pieces with a diameter of 14 mm. The electrodes were dried at 80 °C under vacuum for 12 h to remove all traces of solvent. The 2032-type coin cells were used to prepare lithium metal cells. Celgard 2325 separators (25 μm), 1.2 M LiPF_6 in ethylene carbonate/ethyl methyl carbonate (EC/EMC) (3:7) electrolyte (GEN II with a water content below 20 ppm, 40 μl) and Li metal foil (MTI, 16 mm × 0.6 mm (diameter × thickness), high purity of 99.9%) were used. The half cells were then cycled between 2.0 and 4.8 V versus Li^+/Li , using small amounts of powder (approximately 5.2 mg cm⁻²) as positive electrodes.

The GITT measurements were performed by periodically pulsing and relaxing the battery between 2.0 and 4.8 V using a NEWARE electrochemical analyser with a 10 min pulse at 25 mA g⁻¹ followed by 2 h relaxation for every step. The Li^+ diffusion coefficient (D_{Li^+}) was calculated using equation (1):

$$D_{\text{Li}^+} = \frac{4}{\pi \tau} \left(\frac{R_s}{3} \right)^2 \left(\frac{\Delta E_s}{\Delta E_t} \right)^2 \quad (1)$$

in which τ is the pulse time of 600 s, R_s is the particle equivalent radius of 200 nm, ΔE_s is the steady-state voltage change and ΔE_t is the total voltage change during the current pulse.

BCDI and coherent multiple crystal diffraction

Bragg coherent diffraction data were collected at the 34-ID-C beamline of the Advanced Photon Source (APS). For the coherent diffraction analysis shown in this manuscript, we used 11.2 and 9 keV monochromatic beams in two independent experiments. The coherent X-ray beam was focused using a pair of Kirkpatrick-Baez (KB) mirrors to approximately 1 × 1 μm² illuminating the LMR nanocrystals. The measurement was done on a 10 μm thick LMR electrode in transmission geometry. We used the same in situ coin cell set-up that was implemented in the previous experiments, with a window opening of 1 mm (ref. ³⁹). The coin cell was mounted vertically on a coin cell holder with the LMR electrode located downstream to minimize the absorption of the diffracted X-rays. The particle morphology of the LMR particles was examined with scanning electron microscopy (SEM), indicating 200–600 nm sized LMR particles (Extended Data Fig. 1). From the fringe spacing in the diffraction patterns, we estimated that the measured LMR nanoparticle size is approximately 600 nm. These 3D diffraction patterns of the [003] reflection were analysed using a combination of the error reduction and the hybrid input/output algorithms to reconstruct the 3D structure and the lattice displacement along the momentum transfer direction, which is the particle c axis here.

CMCD patterns were acquired using a Timepix photon-counting detector mounted $D = 1,950$ mm away from the sample. We obtained full rocking curves around the (003) Bragg reflection and collected 2D CMCD patterns using a 2D detector at 2θ angles of 18.6° ($\Delta\theta = \pm 0.15^\circ$), respectively. Although the full sensor of the detector has 512 × 512 pixels with a pixel size of 55 m × 55 m, the coherent diffraction patterns were collected utilizing just the first quadrant sensor, which had fewer bad pixels. Automatic background subtraction was implemented within the detector³⁹. We collected 22 sets of CMCD patterns and each set included 302 CMCD patterns by rocking the sample in 0.0025° steps around the Bragg peak while we were cycling the coin cell at the C/10 current rate (the C/10 rate is the current value discharge of a battery in 20 h). Between consecutive scans, we optimized the sample position on a piezo scanning stage, to maintain the Bragg condition and avoid sample misalignment. The coin cell was cycled using an eight-channel MACCOR battery cycler while the series of measurements progressed.

Synchrotron X-ray diffraction and absorption spectroscopy measurements

Powder diffraction data of the cathode materials were collected using high-energy X-ray diffraction (HEXRD) located at sector 11-ID-C of the APS at Argonne National Laboratory. A high-energy X-ray with a beam size of 0.2 mm × 0.2 mm and wavelength of 0.1173 Å was used to obtain two-dimensional (2D) diffraction patterns in the transmission geometry. X-ray patterns were recorded with a PerkinElmer large-area detector placed at 1,800 mm from the samples. Rietveld refinement of the collected HEXRD patterns was carried out using the GSAS package. Ex situ HEXRD measurements were performed at the same beamline. The electrodes were disassembled from the coin cells charged or discharged to different potentials. With high penetration and low absorption, synchrotron HEXRD precisely reflects bulk sample structure properties, which is beneficial when observing tiny phase changes that are usually invisible in laboratory-scale X-ray diffraction due to poor background noise. To avoid peak interference from the Al current collector, a freestanding LMR electrode was prepared from a mixture of LMR powder, carbon black and polytetrafluoroethylene at 80:10:10 wt% ratios.

X-ray absorption near-edge structure and EXAFS for Mn K edge were performed at the APS on the bending-magnet beamline 9-BM-B. X-ray photon energy was monochromatized by an Si (111) double-crystal monochromator. Higher order harmonic contaminations were eliminated by detuning the monochromator to reduce the incident X-ray

Article

intensity by approximately 30%. All spectra were collected at room temperature in the transmission mode.

DFT calculation

All calculations were performed based on DFT using the plane-wave projector-augmented wave method, as implemented in the Vienna ab initio simulation package. The Perdew–Burke–Ernzerhof (PBE) exchange-correlation functional was used and the Hubbard U corrections (PBE+U) were taken into account, with the effective U of Mn (4.2 eV) adopted from previous studies. A kinetic energy cut-off of 520 eV and a k-point mesh of $11 \times 11 \times 11$ were used. Spin polarization was considered for all calculations. Structures were relaxed until a force tolerance of 0.01 eV Å⁻¹ was reached. The formation energy (E^f) of oxygen vacancy was obtained using the following formula:

$$E^f[V_O] = E_{\text{total}}[V_O] - E_{\text{total}}[P] + \mu_O$$

where $E_{\text{total}}[V_O]$ and $E_{\text{total}}[P]$ are the total energies of the supercells with and without an oxygen vacancy, respectively. μ_O is the chemical potential of oxygen, for which we used the gas phase O₂ molecule as the reference. An energy correction of 0.68 eV per atom was applied to compensate the overbinding of O₂ in DFT calculations.

Gas evolution analysis

DEMS was applied to detect and identify gas evolution of different cathode materials during first charge/discharge. The DEMS was built based on a purchased mass spectrometer (HPR-40, Hiden Analytical). A home-made cell with glass fibre separators and 1.2 M LiPF₆ in EC/EMC (3:7) electrolyte (GEN II) was used for *in situ* measurements. To increase the gas detection accuracy, we adopted the method of intermittent gas intake and used a certain degree of vacuum to ensure that the generated gas was completely ingested. The generated gas was collected in the cell for 60 min before being ingested into the mass spectrometer. In addition, to prevent O₂ from reacting with Li metal, we assembled full cells using graphite as the anode electrode in our DEMS experiments. The cells were then cycled at a current rate of C/10 between 2.0 and 4.8 V versus Li⁺/Li, using small amounts of powders (approximately 8 mg) as positive electrodes.

TEM measurement

TEM and HRTEM were conducted using the Argonne chromatic aberration-corrected TEM (ACAT) (a FEI Titan 80–300ST with an image

aberration corrector to compensate for both spherical and chromatic aberrations) at an accelerating voltage of 200 kV. The 3D-rED datasets were acquired by stepwise tilting the sample with a collection angle of -40° to 40° . The tilt step was 2° . The reciprocal lattice pattern was then reconstructed using a Python script and the RED processing software package developed by Wan et al.⁵⁰. The script can be downloaded from https://github.com/danielzt12/EDiff_3D_projection/.

Data availability

The data that support the findings of this study are available from the corresponding authors upon request.

50. Wan, W., Sun, J., Su, J., Hovmöller, S. & Zou, X. Three-dimensional rotation electron diffraction: software RED for automated data collection and data processing. *J. Appl. Crystallogr.* **46**, 1863–1873 (2013).

Acknowledgements We gratefully acknowledge support from the US Department of Energy (DOE), Office of Energy Efficiency and Renewable Energy, Vehicle Technologies Office. This work was also supported by the Clean Vehicles, US–China Clean Energy Research Centre (CERC-CVC2) under US DOE EERE Vehicle Technologies Office. Argonne National Laboratory is operated for DOE Office of Science by UChicago Argonne, LLC, under contract number DE-AC02-06CH11357. This research was also supported by the National Key R&D Program of China (2016YFB0700600), Soft Science Research Project of Guangdong Province (no. 2017B030301013) and the Shenzhen Science and Technology Research Grants (no. ZDSYS201707281026184). This research used resources of the Advanced Photon Source (11-ID-C, 9BM and 34-ID-C), a US DOE Office of Science User Facility operated for the DOE Office of Science by Argonne National Laboratory under contract no. DE-AC02-06CH11357. Work at Brookhaven National Laboratory was supported by the DOE, Office of Science, Office of Basic Energy Sciences, under contract no. DE-SC0012704. Electron microscopy was carried out at the Center for Nanoscale Materials, an Office of Science user facility, supported by the US Department of Energy, Office of Science, Office of Basic Energy Sciences, under contract no. DE-AC02-06CH11357.

Author contributions T.L., J. Liu, L.L., J. Lu, F.P. and K.A. conceived the idea and designed the experiments. T.L., J. Liu, R.Q. and S.X. synthesized all the materials and conducted electrochemical measurements. J. Liu, L.Y., T.Z., Y.X., W.Z. and J.W. carried out the TEM, EELS and 3D-rED measurements. T.L., A.D., T.W., L.W. and Y.R. performed ex situ synchrotron HEXRD and XAS. T.L., L.L., J.D., W.C., R.H. and I.R. performed *in situ* BCDI, CMCD and data analysis. S.L., J.Z. and F.P. conducted DFT calculation. T.L., J. Liu, J. Lu, F.P. and K.A. wrote the manuscript and all authors edited the manuscript.

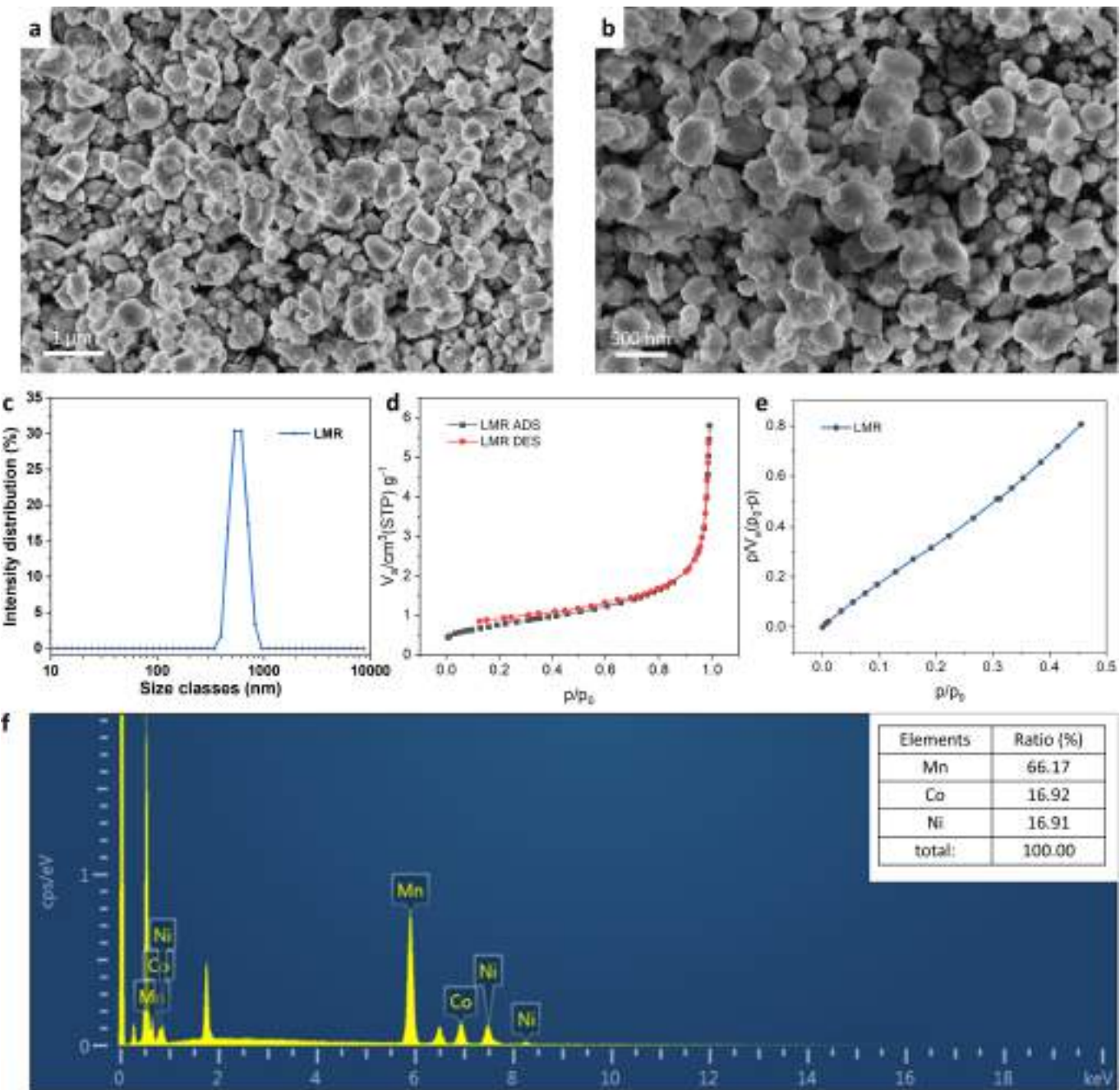
Competing interests The authors declare no competing interests.

Additional information

Correspondence and requests for materials should be addressed to Jun Lu, Feng Pan or Khalil Amine.

Peer review information *Nature* thanks Doron Aurbach and the other, anonymous, reviewer(s) for their contribution to the peer review of this work.

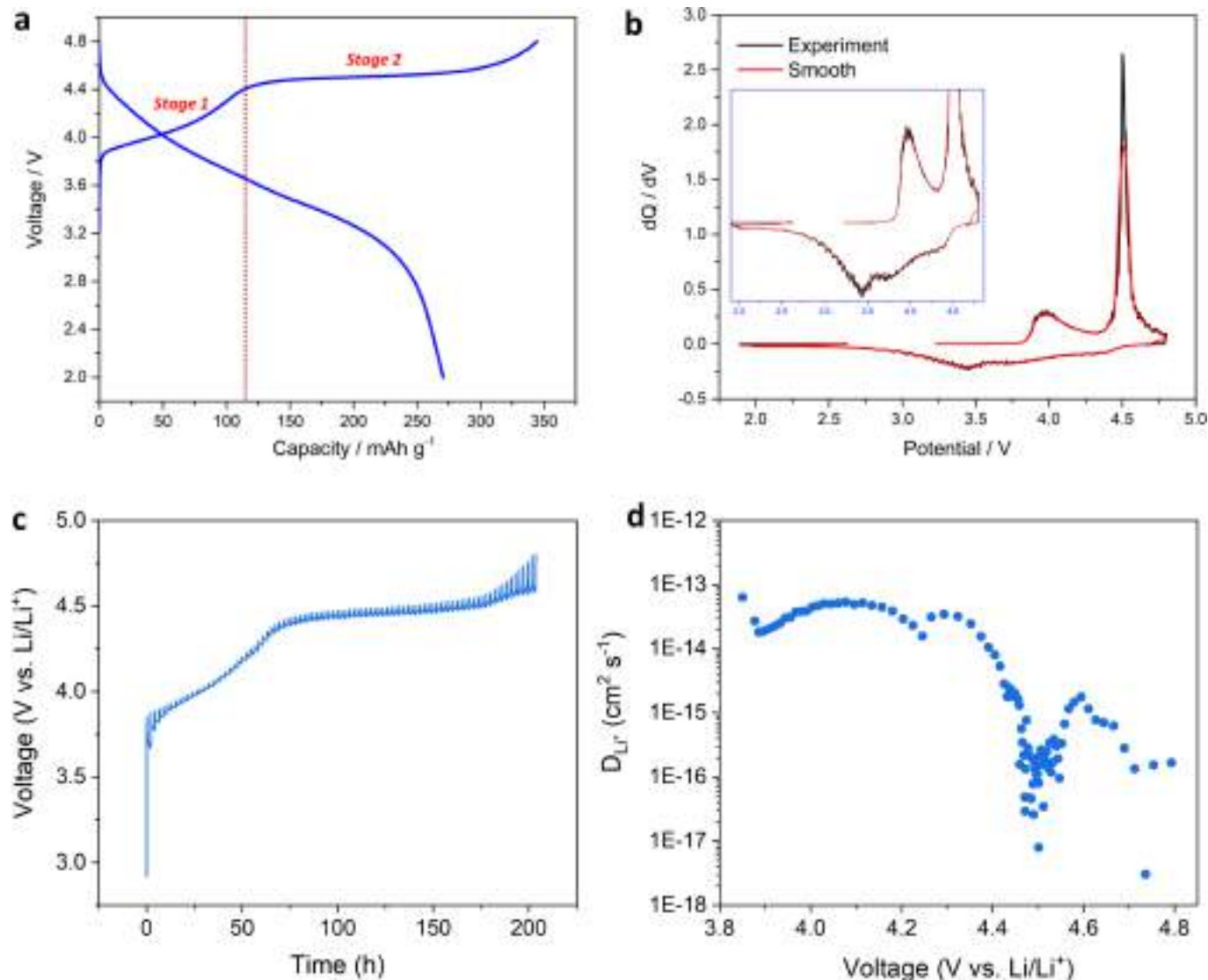
Reprints and permissions information is available at <http://www.nature.com/reprints>.



Extended Data Fig. 1 | The morphology, particle distribution, surface area and composition of the LMR cathode. **a, b** The SEM image of the LMR powder. The particle size ranges from 200–600 nm. **c** The particle size distribution of the as-prepared LMR cathode. The mean particle size of LMR cathode is around 583 nm. **d** The nitrogen adsorption/desorption isotherm of LMR. **e** The

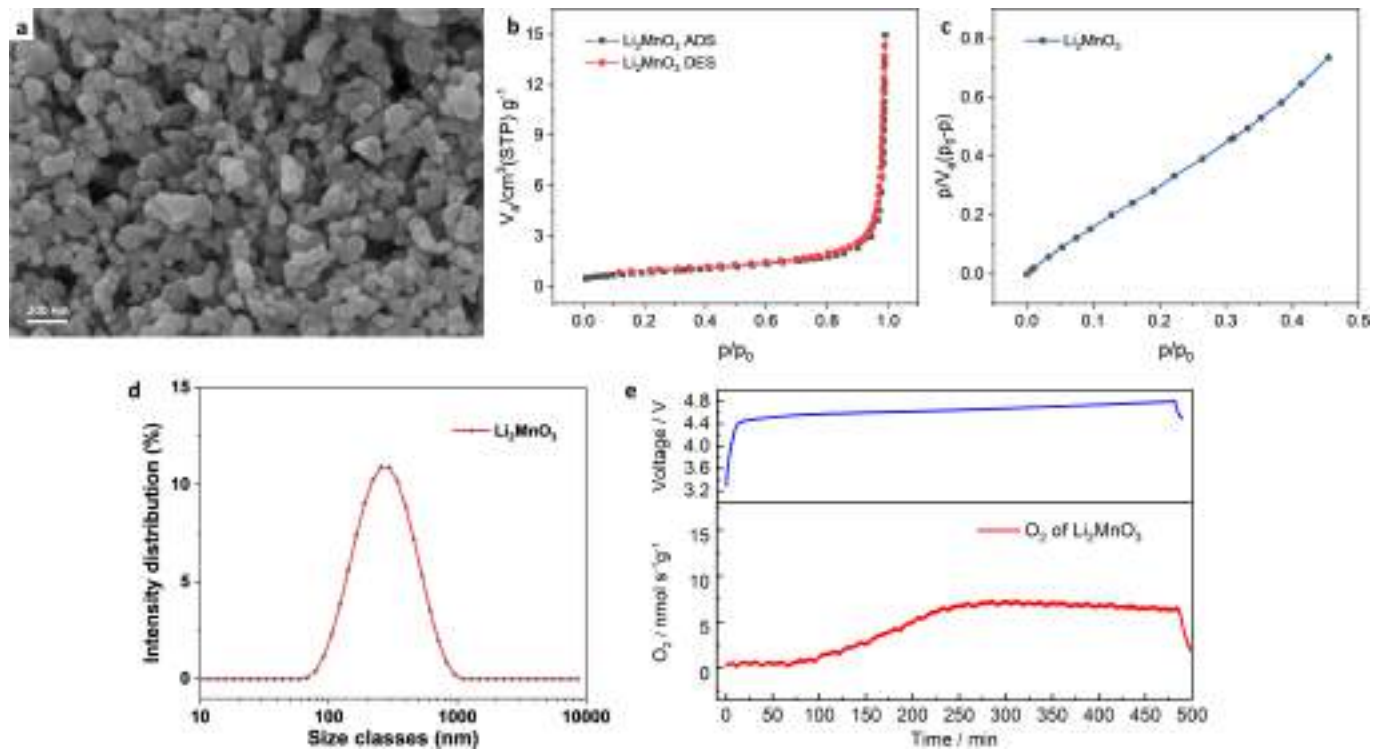
corresponding BET plot of LMR. The nitrogen adsorption/desorption isotherm and the corresponding BET plot of the as-prepared LMR cathode indicate that its specific surface area is calculated to be $2.804 \text{ m}^2 \text{ g}^{-1}$. **f** SEM-EDS results of the pristine LMR cathode. The actual chemical composition complies well with the design ($\text{Mn}:\text{Co}:\text{Ni} = 4:1:1$).

Article



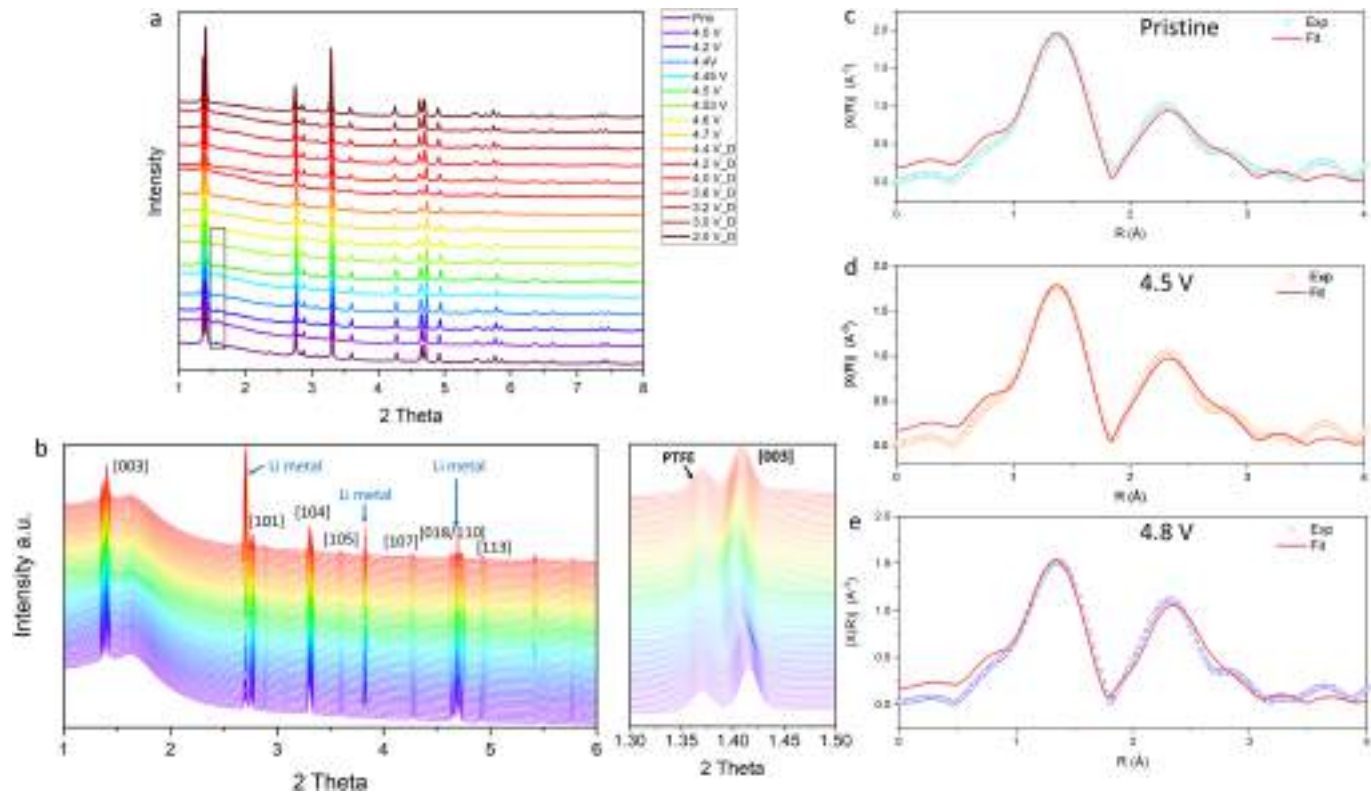
Extended Data Fig. 2 | The electrochemical properties of the LMR cathode. **a, b** The first charge/discharge curve and corresponding dQ/dV curve of LMR cathode. The first charge profile exhibits two distinct electrochemical stages at different voltage ranges. Stage 1 corresponds to the Li^{+} extraction (de-lithiation) from $LiTMO_2$ domains with concomitant oxidation of Ni^{2+} and Co^{3+} . Stage 2 corresponds to the activation of Li_2MnO_3 domains, further Li^{+}

extraction and at this stage oxygen is oxidized (at high potentials) to per-oxo species: $(2O^{2-} \leftrightarrow [O_2]^{2-} + 2e^-)$. **c, d** The galvanostatic intermittent titration technique (GITT) test of the first charge. The Li-ion diffusion coefficient keeps stable in stage 1 but dramatically decreases after the activation of Li_2MnO_3 domains (stage 2).



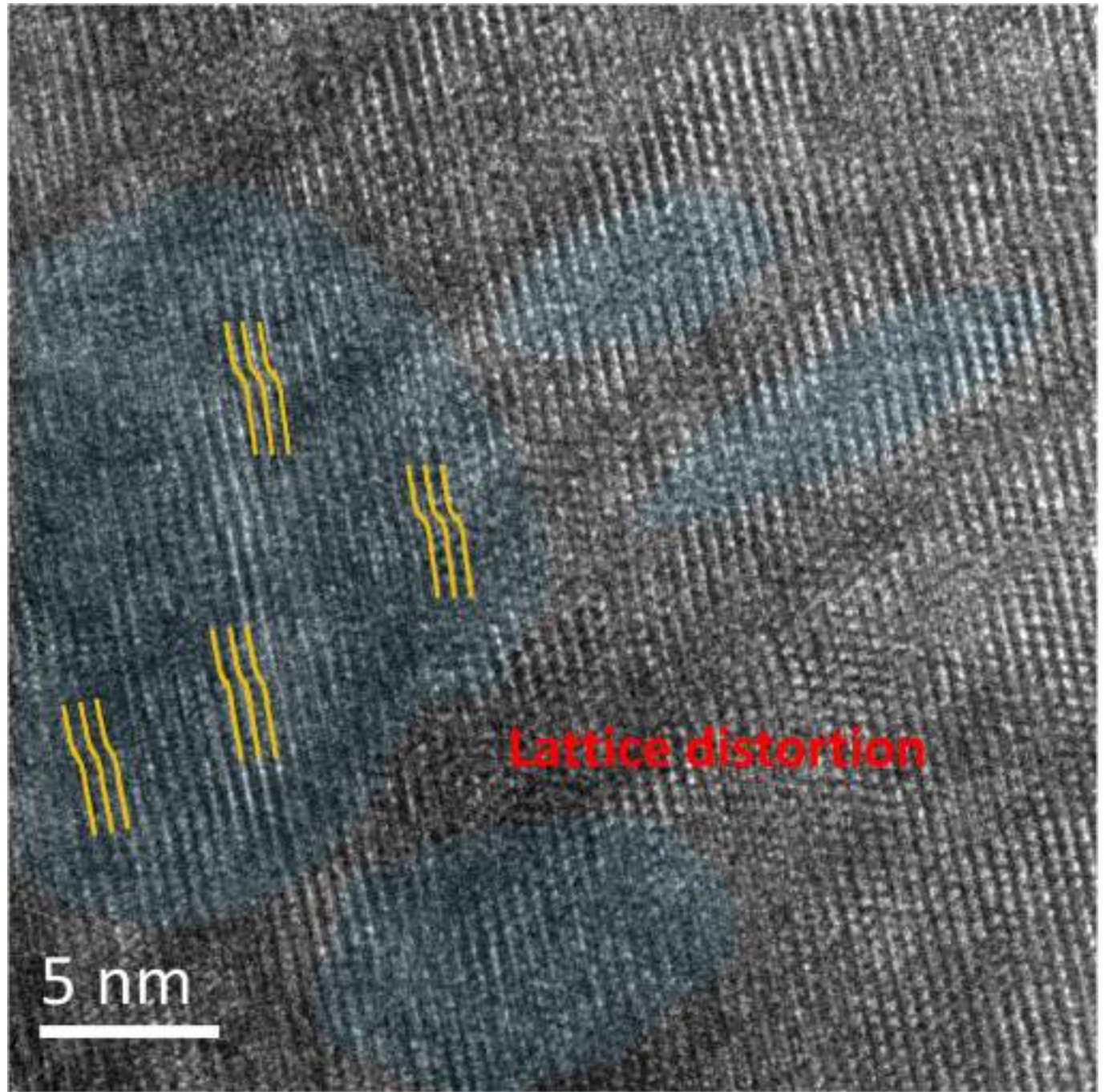
Extended Data Fig. 3 | The morphology, particle distribution, surface area and in situ DEMS of the Li_2MnO_3 cathode. **a** The SEM image of the as-prepared Li_2MnO_3 powder. The as-prepared Li_2MnO_3 exhibits a single-particle morphology with average particle size of 100–200 nm. **b** The nitrogen adsorption/desorption isotherm of the as-prepared Li_2MnO_3 powder. **c** The

corresponding BET plot of the as-prepared Li_2MnO_3 powder. The specific surface area of Li_2MnO_3 is calculated to be $3.1106 \text{ m}^2 \text{ g}^{-1}$. **d** The particle size distribution of the as-prepared Li_2MnO_3 powder. **e** In situ DEMS for the first charge of Li_2MnO_3 . The signal of O_2 evolution is not detected until 20% delithiation of Li_2MnO_3 .



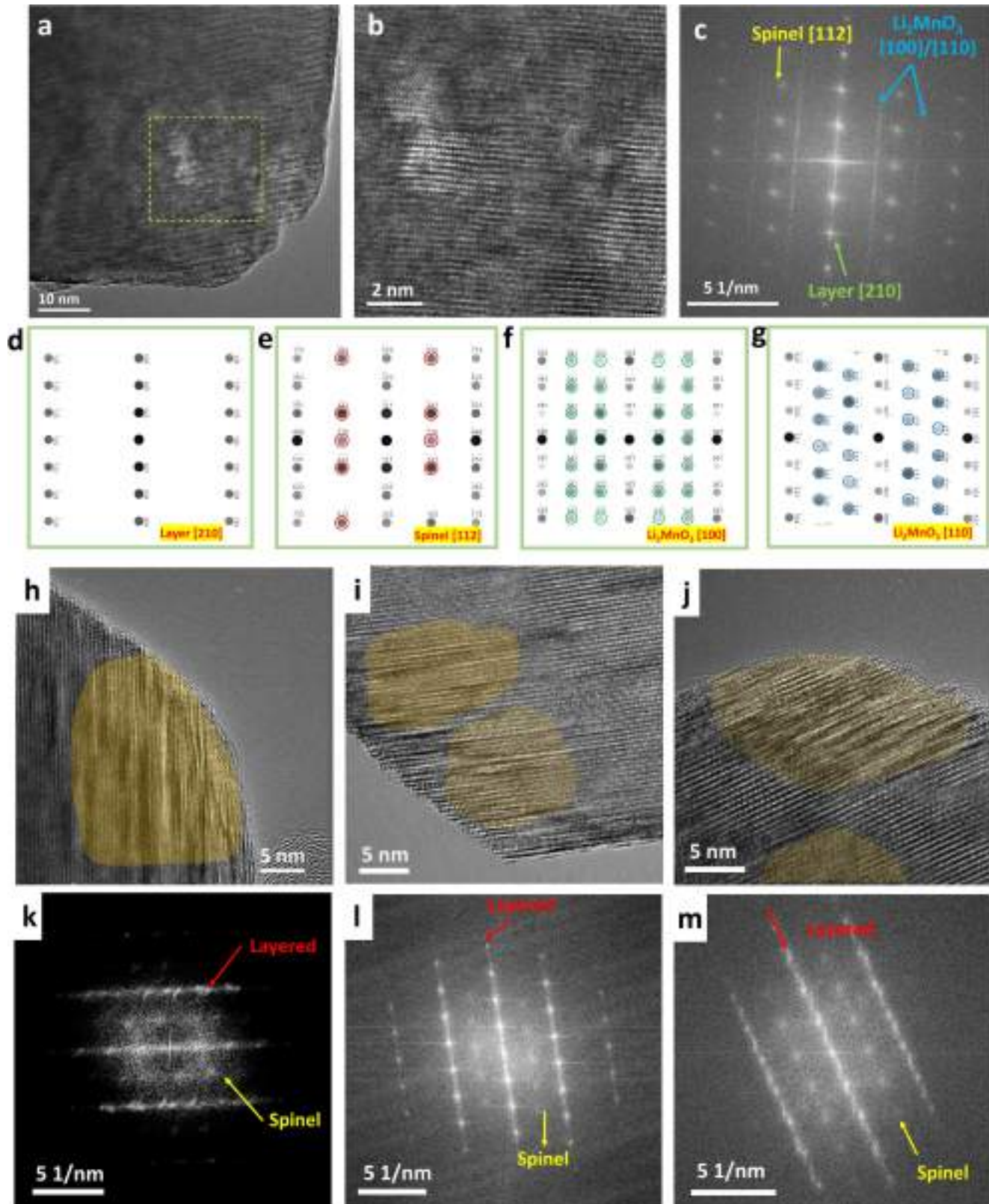
Extended Data Fig. 4 | The ex situ and in situ XRD and ex situ XAS of the LMR cathode. **a** The ex situ XRD patterns of the first charge/discharge for the LMR cathode. The superlattice evolution of the LMR cathode can be observed in the 2 theta range of 1.5–1.8°. The obvious lattice parameter changes can be observed from ex situ XRD pattern, particularly in the 2 theta range of 3.0–6.0°. **b** The in situ XRD patterns of the as-prepared LMR cathode during the first charge/discharge in the voltage range of 2.0–4.8 V using a current rate of C/10

($1C = 250 \text{ mA g}^{-1}$). The obvious lattice parameter changes can be observed from in situ XRD patterns, particularly in the 2 theta range of 1.3–1.5°. Generally, the structure evolution observed in in situ XRD is completely consistent with that in ex situ XRD (Figure 3c). **c–e** Ex situ Mn K-edge EXAFS spectra of the samples at pristine, 4.5V and 4.8V and the corresponding fitting results. Detailed fitting results are shown in Extended Data Table 2.



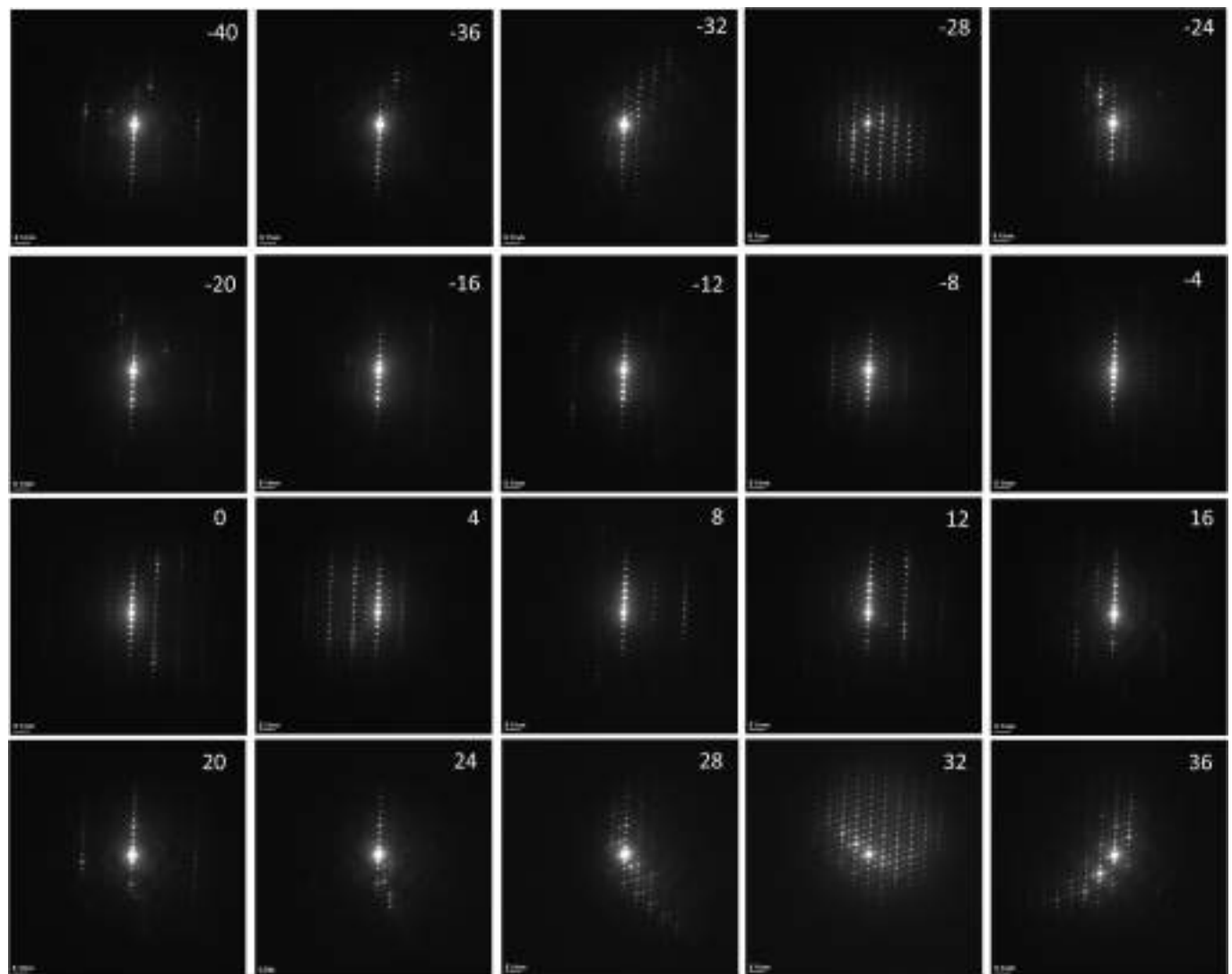
Extended Data Fig. 5 | Visible lattice displacement observations using TEM of the LMR charged to 4.47 V. High magnification TEM image of the LMR charged to 4.47 V. Although the layered structure is maintained, lattices in the marked areas are deformed significantly.

Article

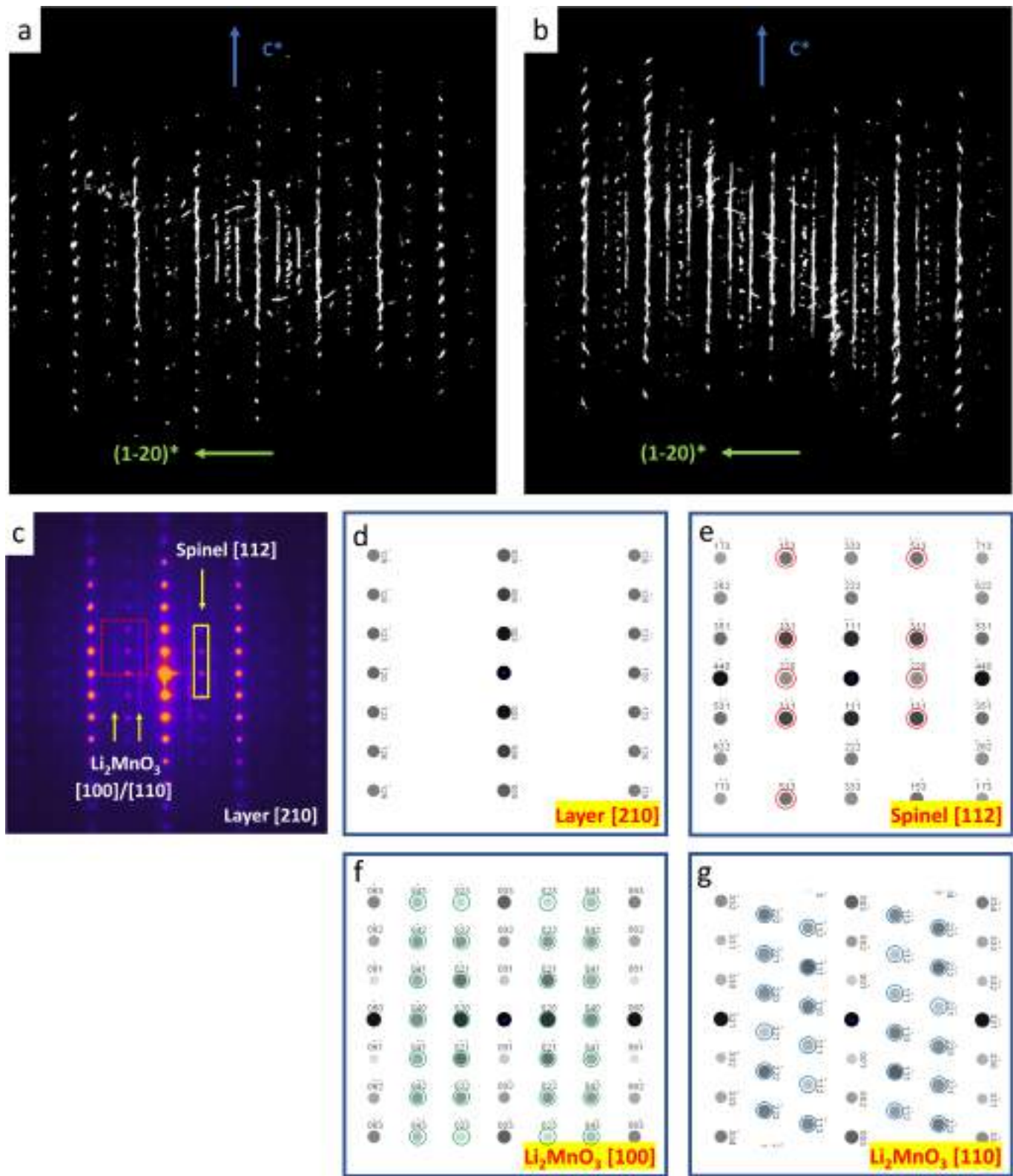


Extended Data Fig. 6 | Visible structural observations of the LMR charged to 4.5 V. **a** High magnification TEM image of the LMR charged to 4.5 V. **b** The enlarged image of the selected area in Extended Data Fig. 6a. **c** The corresponding Fourier pattern of the select area of Extended Data Fig. 6a. **d, e, f** and **g** The simulated patterns of standard electron diffractions for layer [210], spinel [112], and Li_2MnO_3 [100]/[110]. **h, i** and **j** TEM images of the LMR

cathode charged to 4.5 V. The lattice displacements are highlighted with yellow marks. **k, l** and **m** The corresponding FFT images of Extended Data Fig. 6h, i and j. Obvious lattice displacements are observed in the different particles and the corresponding FFT images confirm the existence of spinel phase at 4.5 V, which is highly consistent with Fig. 4g results.

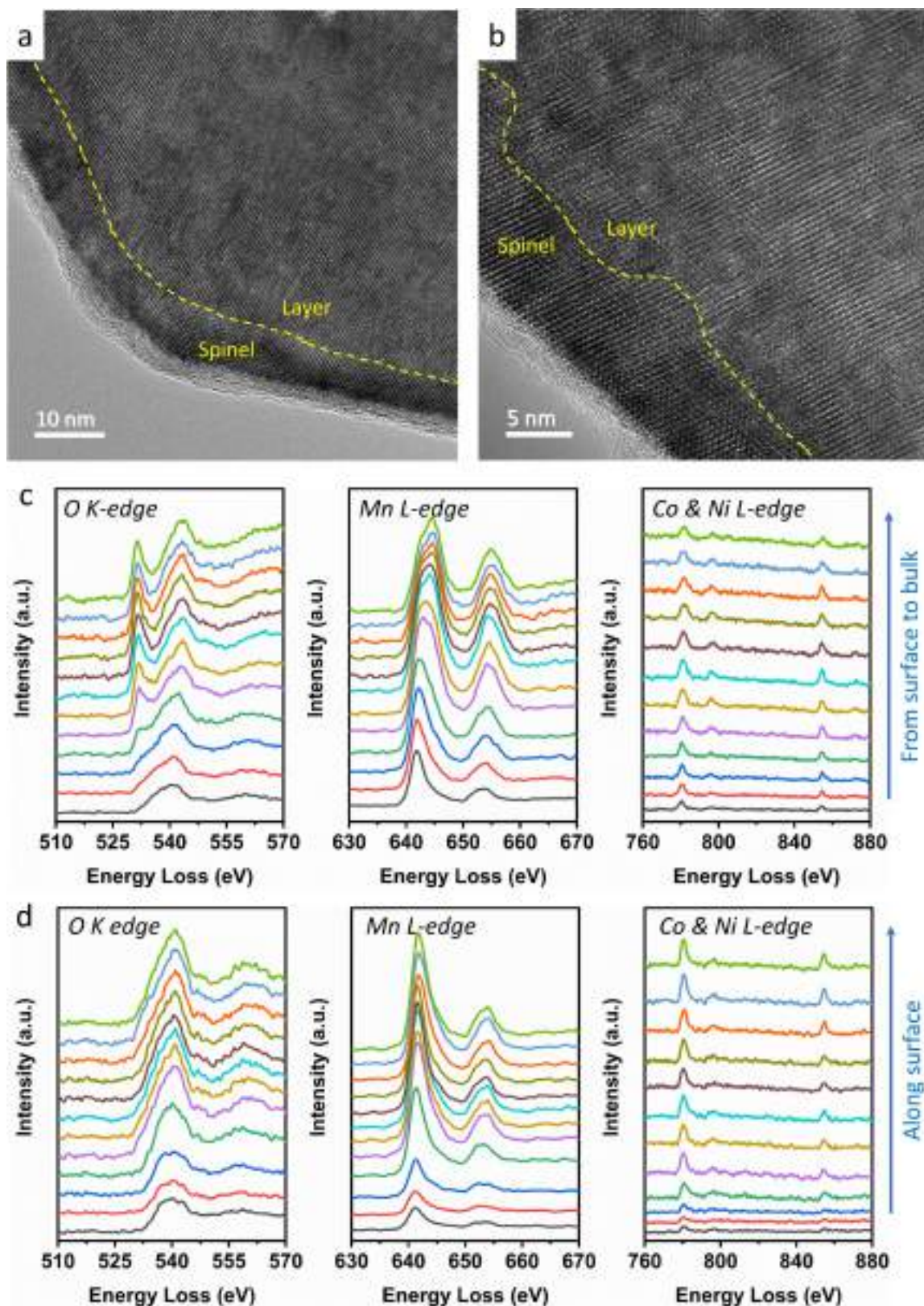


Extended Data Fig. 7 | The SAED images captured at different rotation angles from -40 to 36° . These SAED images in Extended Data Fig. 7 are used for 3D-rED reconstruction present in Fig. 4e–f.



Extended Data Fig. 8 | Lattice displacement and structure changes observed from 3D-rED and SAED. **a, b** The reciprocal lattice viewed along the a^* axis of the LMR cathode at 4.5 V. **c** The selected area electron diffraction (SAED) image of the sample charged to 4.5 V. In addition to the typical layered

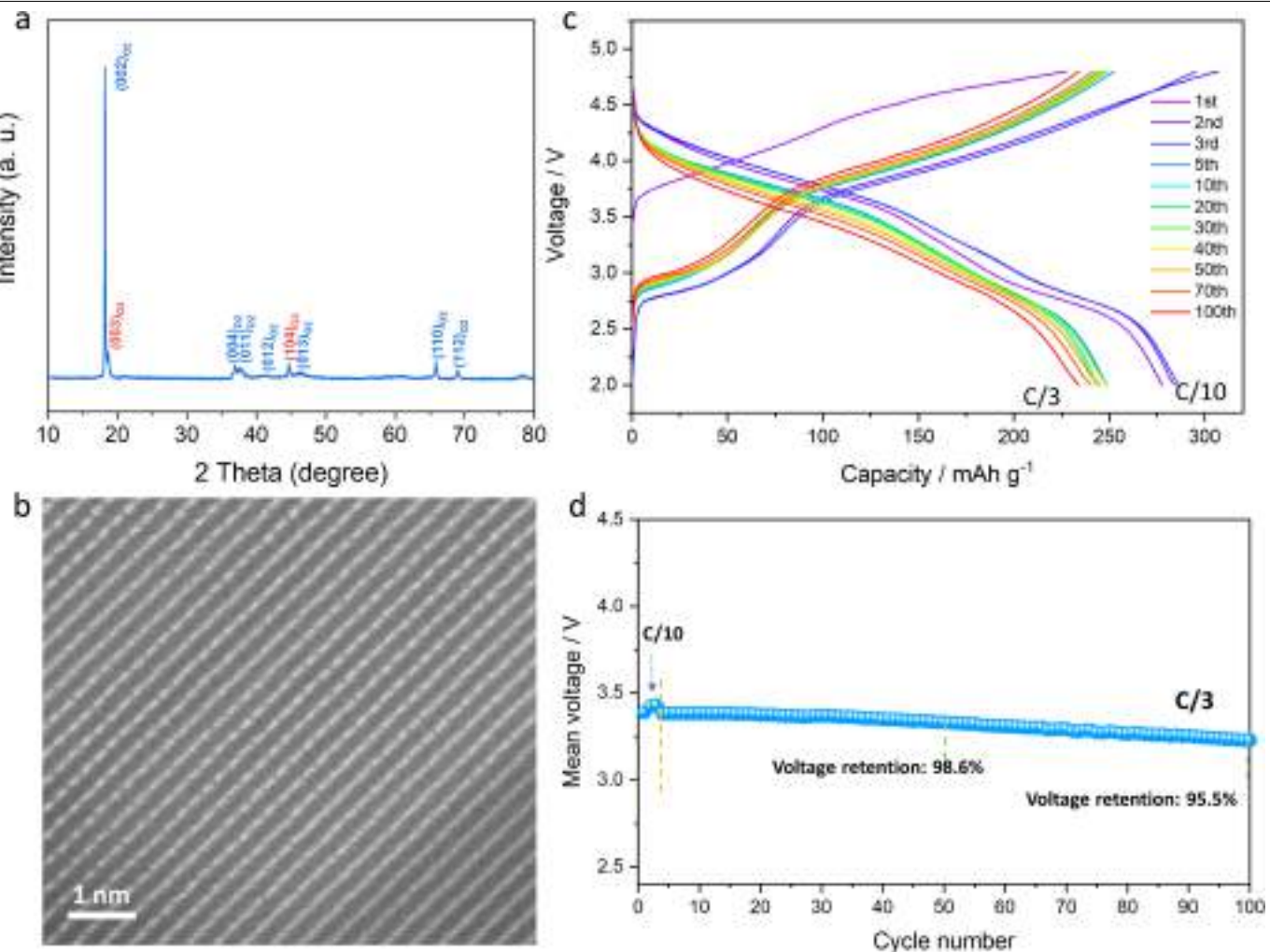
structure and weak Li_2MnO_3 reflection, the reflection that corresponds to the spinel lattice can be also observed. **d, e, f** and **g** The simulated patterns of standard electron diffractions for Layer [210], spinel [112], and Li_2MnO_3 [100]/[110].



Extended Data Fig. 9 | Visible structural observations and chemical state changes of the LMR charged to 4.8 V. **a, b** Low and High magnification TEM image of the LMR charged to 4.8 V. A clear reconstruction surface layer with the spinel phase can be visualized. **c** Electron energy loss spectroscopy line scans of the O K-edge, Mn L-edge, Co & Ni L-edge for the LMR charged to 4.8 V along the direction from surface to bulk. The intensity of O-K edge pre-peaks

substantially reduces from the interior to the exterior and almost disappears near the surface. Concurrently, Mn L-edge shows left shift near the surface.

d Electron energy loss spectroscopy line scans of the O K-edge, Mn L-edge, Co & Ni L-edge for the LMR charged to 4.8 V along the surface fringe. The O-K line-scan parallel to the surface confirms that the oxygen release uniformly occurs in the entire particle surface as the disappeared O pre-peak.



Extended Data Fig. 10 | Structure and electrochemical properties of O2 phase-based LMR. **a** The XRD pattern of as-prepared $\text{Li}_x\text{Ni}_{0.13}\text{Mn}_{0.54}\text{Co}_{0.13}\text{O}_2$. The diffraction peaks belonging to an O2 phase with P63mc symmetry are indexed by blue marks, while some tiny peaks belonging to O3 phase with R-3m symmetry are indexed by red marks. **b** High-resolution TEM image showing the atomic arrangements of O2 phase LMR. The Li_2MnO_3 -like domain is rarely observed in the O2-type LMR, which suggests that the Li@Mn₆ structural motifs in the O2 type LMR cathode are dispersed in the TM layer instead of

being aggregated to form a Li_2MnO_3 -like domain. **c** The charge/discharge profiles of O2 phase-based LMR cathode. The cells were activated at C/10 within first 3 cycles and then cycled at C/3. The smooth charging behaviour with no apparently differentiated voltage plateaus indicates effectively suppressed differential electrochemical activities. **d** The voltage stability of the O2 type LMR cathode during cycles presents in the plot of average (mean) voltage profiles vs cycle number.

Extended Data Table 1 | Lattice parameters obtained by the two-phase structure model refinement of pristine LMR cathode

Phases		Phase fraction	0.57(4)
Phase 1 Space group: $R\bar{3}m$	Lattice parameters	$a=b$	2.8535(6) (Å)
		c	14.2424(9) (Å)
		V	100.43(6) (Å ³)
Phase fraction		0.43(4)	
Phase 2 Space group: $C2/m$	Lattice parameters	a	4.9488(1) (Å)
		b	8.5485(4) (Å)
		c	5.0366(6) (Å)
		β	109.556(0) (°)
Agreement factors		V	200.78(2) (Å ³)
		Rwp (%)	5.73
		Rp (%)	5.86

The XRD pattern of the LMR cathode is refined using the two-phase model, which consists of both rhombohedral $R\bar{3}m$ and monoclinic $C2/m$ phases that are present in LMR cathodes.

Article

Extended Data Table 2 | Structural parameters of the samples obtained by fitting the EXAFS data

Samples	Shells	CN	R (Å)	σ^2 (Å ²)	ΔE (eV)	R-Factor
pristine	Mn-O	6	1.905	0.003	-5.3	0.014
	Mn-TM	2.8	2.869	0.003		
charged to 4.5 V	Mn-O	5.3	1.904	0.003	-4.7	0.010
	Mn-TM	2.7	2.873	0.003		
charged to 4.8 V	Mn-O	4.9	1.890	0.005	-7.7	0.015
	Mn-TM	3.8	2.875	0.005		

There are the average coordination number (CN), path distance (R), Debye-Waller factor (σ^2), threshold energy correction (ΔE), and the R-Factor of the fitting.